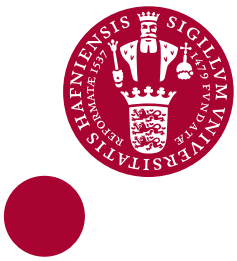

A model-based insight into the coupling of nitrogen and sulfur cycles in a coastal upwelling system

Muchamad, Al Azhar; Canfield, Donald E.; Fennel, Katja; Thamdrup, Bo; Bjerrum, Christian J.

Published in:
Journal of Geophysical Research: Biogeosciences

DOI:
10.1002/2012JG002271

Publication date:
2014

Document version
Publisher's PDF, also known as Version of record

AGU PUBLICATIONS

JGR

Journal of Geophysical Research: Biogeosciences

RESEARCH ARTICLE
10.1002/2012JG002271

Key Points:
- New biogeochemical submodule in the Regional Ocean Model System is presented
- Coupled nitrogen and sulfur cycles in a coastal upwelling system is analyzed
- Significant contribution of nitrate and sulfate reduction to remineralizations

Supporting Information:
- Supporting information
- Supporting information

Correspondence to:
M. A. Azhar,
azhar.al@gmail.com

Citation:
Azhar, M. A., D. E. Canfield, K. Fennel, B. Thamdrup, and C. J. Bjerrum (2014), A model-based insight into the coupling of nitrogen and sulfur cycles in a coastal upwelling system, *J. Geophys. Res. Biogeosci.*, *119*, 264–285, doi:10.1002/2012JG002271.

Received 22 DEC 2012
Accepted 7 DEC 2013
Accepted article online 19 FEB 2014
Published online 19 MAR 2014

A model-based insight into the coupling of nitrogen and sulfur cycles in a coastal upwelling system

Muchamad Al Azhar[1], Donald E. Canfield[2], Katja Fennel[3], Bo Thamdrup[2], and Christian J. Bjerrum[1]

[1]Nordic Center for Earth Evolution (NordCEE) and Department of Geosciences and Natural Resource Management, University of Copenhagen, København K, Denmark, [2]Nordic Center for Earth Evolution (NordCEE) and Institute of Biology, University of Southern Denmark, Odense M, Denmark, [3]Department of Oceanography, Dalhousie University, Halifax, Nova Scotia, Canada

Abstract The biogeochemical cycling in oxygen-minimum zones (OMZs) is dominated by the interactions of microbial nitrogen transformations and, as recently observed in the Chilean upwelling system, also through the energetically less favorable remineralization of sulfate reduction. The latter process is masked, however, by rapid sulfide oxidation, most likely through nitrate reduction. Thus, the cryptic sulfur cycle links with the nitrogen cycle in OMZ settings. Here, we model the physical-chemical water column structure and the observed process rates as driven by formation and sinking of organic detritus, to quantify the nitrogen and sulfur cycles in the Chilean OMZ. A new biogeochemical submodule was developed and coupled to the Regional Ocean Model System (ROMS). The model results generally agree with the observed distribution of reactive species and the measured process rates. Modeled heterotrophic nitrate reduction and sulfate reduction are responsible for 47% and 36%, respectively, of organic remineralization in a 150 m deep zone below mixed layer. Anammox contributes to 61% of the fixed nitrogen lost to N_2 gas, while the rest of the loss is through canonical denitrification as a combination of organic matter oxidation by nitrite reduction and sulfide-driven denitrification. Mineralization coupled to heterotrophic nitrate reduction supplies ~48% of the ammonium required by anammox. Due to active sulfate reduction, model results suggest that sulfide-driven denitrification contributes to 36% of the nitrogen loss as N_2 gas. Our model results highlight the importance of considering the coupled nitrogen and sulfur cycle in examining open-ocean anoxic processes under present, past, and future conditions.

1. Introduction

The surface waters of coastal upwelling systems receive an abundant nutrient supply from deeper waters driven by alongshore winds and offshore water mass transport [*Csanady*, 1990]. The intense biological activity in the photic zone of such systems results in a high export of organic carbon to the deep waters [*Barber and Smith*, 1981]. In combination with large-scale ocean circulation, decomposition of this exported organic matter intensifies the depletion of oxygen at midwater depths, producing the so-called oxygen minimum zone (OMZ). OMZs with negligible oxygen are located in the upwelling areas of Chile-Peru, California, Benguela, and in the Arabian Sea [*Kamykowski and Zentara*, 1990; *Paulmier and Ruiz-Pino*, 2009].

Classically, both geochemical observations and models of OMZ chemistry have focused on the nitrogen cycle, and in particular, nitrogen loss through heterotrophic denitrification during organic matter remineralization under low-oxygen conditions at midwater depths [*Codispoti and Richards*, 1976; *Chapman and Shannon*, 1985; *Gruber and Sarmiento*, 1997; *Canfield*, 2006]. This picture changed with the recognition of the anammox process (anaerobic oxidation of ammonium) as a significant, if not dominant, pathway of N_2 formation in OMZs [*Dalsgaard et al.*, 2003; *Thamdrup et al.*, 2006; *Lam et al.*, 2009]. However, even with these advances, it was not suspected that there would be a role for organic carbon remineralization in OMZs by sulfate reduction. A recent study by *Canfield et al.* [2010] in the northern Chilean upwelling system revealed that sulfate reduction contributed to a surprisingly large proportion of the organic matter remineralization. Sulfate reduction leads to a cryptic sulfur cycle, where sulfate is actively reduced and rapidly re-oxidized again, in the nitrate and nitrite-rich oxygen-free waters. The recognition of this cryptic sulfur cycle in the Chilean upwelling system makes this OMZ a compelling model system for quantitatively exploring the coupling between the sulfur, nitrogen, and organic carbon cycles.

To further this goal, modeling can also reveal the relative balance between nitrate reduction to nitrite, and nitrite reduction to N_2, including denitrification and anammox. Thus, through modeling, we can put

quantitative constraints on the processes of organic matter oxidation as well as the pathways of nitrogen transformation including the sources of ammonium for anammox, issues which have been the source of great uncertainty [*Thamdrup et al*., 2006; *Ward et al*., 2007; *Lam et al*., 2009]. A well-calibrated model platform can also be used to broadly assess the role of the sulfur and nitrogen cycles in present-day OMZs, as well as those in geological past and those which will develop in projected ocean warming scenarios.

Here, we employ a coupled physical and biogeochemical regional ocean model to investigate the dynamics of element cycling in OMZ waters of the Chilean coastal upwelling system. We use the Regional Ocean Modeling System (ROMS) in a three-dimensional idealized physical configuration with a high resolution where mesoscale eddy features are adequately captured [www.myroms.org; *Shchepetkin and McWilliams*, 2005; *Haidvogel et al*., 2008]. We used an idealized coastal setup and boundary conditions to assess the model robustness in simulating present-day first-order biogeochemical cycling in the OMZ. We develop and describe a new ROMS submodule for kinetic modeling of the nitrogen, phosphate, oxygen, and sulfur cycles, building on the work by *Soetaert et al*. [1996], *Fennel et al*. [2006, 2002], *Konovalov et al*. [2006], and *Jensen et al*. [2009]. Together with horizontal and vertical advection, and mixing, the biogeochemical model captures important processes in the low-oxygen ocean by resolving rates of oxic remineralization, heterotrophic nitrate reduction to nitrite, heterotrophic denitrification (i.e., organic matter oxidation by nitrite), sulfate reduction, nitrification of ammonium and nitrite, anammox, and sulfide oxidation by oxygen, nitrate, and nitrite. The schematic of the biogeochemical model is presented in Figure 1.

2. Model Descriptions

The OMZ of the Chile upwelling system is modeled with the three-dimensional ROMS ocean circulation and coupled to our novel modification and expansion of the nitrogen-based biogeochemical submodule which previously was developed by *Fennel et al*. [2006] and *Fennel et al*. [2013].

2.1. Physical Model

The ROMS model solves the free surface hydrostatic primitive equations with a third-order upstream and fourth-order centered scheme for horizontal and vertical advection, respectively. Here, the K-profile parameterization is used for surface and bottom boundary layer mixing [*Large et al*., 1994].

An idealized configuration is used to test the general robustness of the model in capturing the present-day first-order aspect of the biogeochemistry of coastal upwelling systems exemplified by the northern Chilean system. The model is set with a straight coastline as the eastern boundary and flat and uniform bottom topography of 1000 m. The rectangular domain consists of 1200 km zonal width and 1600 km meridional extension so possible model artifacts of the open boundaries do not reach the model interior. The horizontal resolution is 1/8 degree in order to capture the mesoscale dynamics of upwelling systems such as eddies and filaments (Figure 2). The layer thickness varies from 2.5 m at the surface to 100 m at the bottom in the 30 levels of vertical sigma-coordinate system.

Monthly forcing of wind stress and heat fluxes from the COADS climatology are set to be spatially uniform based on average values for the region between 15°S and 25°S of the northern Chilean coast. This monthly forcing reproduces the differences in upwelling strength that are necessary to capture seasonal variations in biological activity [cf. *Carr and Kearns*, 2003]. Open lateral boundary conditions of sea surface height, velocity, temperature, and salinity are imposed at the northern, southern, and western boundaries. The baroclinic velocity is generated from a geostrophic current approximation [*Jin et al*., 2009]. Radiation conditions for depth-averaged velocity [*Flather*, 1976] and sea surface height [*Chapman*, 1985] are applied to radiate out gravity waves generated within the model domain. A sponge layer, where harmonic horizontal viscosity and diffusivity increase as a function of half cosine function, is used to dampen propagation of artificial inertial waves into the model domain [*Marchesiello et al*., 2001]. The values are set to vary linearly from 100 $m^2\ s^{-1}$ at the open boundary to zero at approximately 130 km from the boundary. These values are added to the harmonic horizontal viscosity and diffusivity background values of 10 and 5 $m^2\ s^{-1}$, respectively, which are used in the entire domain.

Initial and open boundary values of temperature and salinity were derived using an analytical formulation fit to *RV AGOR-60 Vidal Gormaz* cruise data from the northern Chilean coast (off Iquique ~ 20°S) in August 2009 and January 2010. These initial values are set to be spatially uniform, except for an approximately 0.3°C

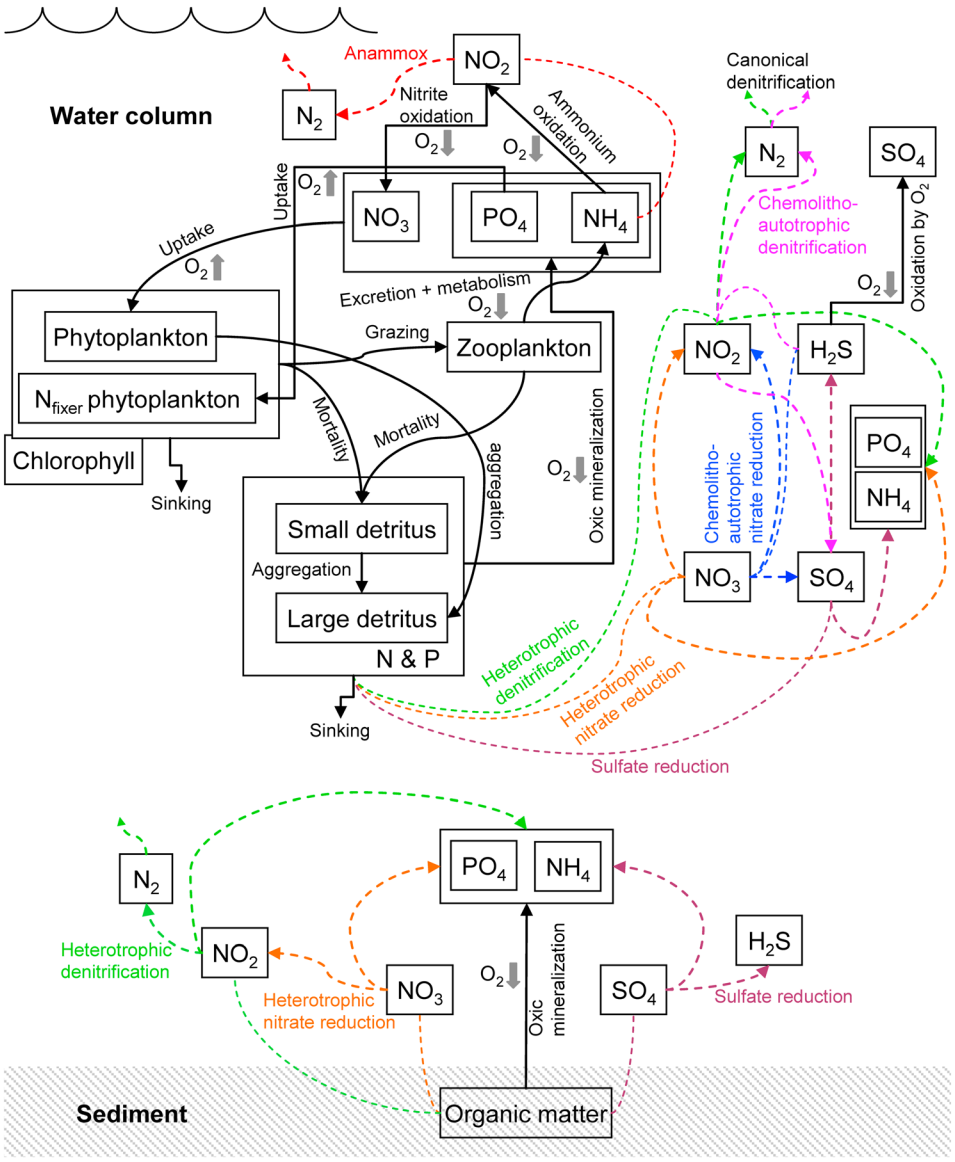

Figure 1. Flow diagram of the ecosystem-biogeochemical model. The model consists of 14 state variables (see Appendixes for detail). Anaerobic processes of remineralization and oxidation are highlighted by dashed lines. Processes which produce (consume) oxygen are indicated by up (down) gray thick arrows. It is worth to note that canonical denitrification is the sum of heterotrophic denitrification and sulfide-driven denitrification. Organic matter that reaches the seafloor is assumed to be remineralized instantaneously by oxic and/or anoxic remineralizations.

decrease in temperature from north to south in the upper 200 m depth and an upward thermocline that tilts toward the coast to generate the geostrophic poleward undercurrents [*Jin et al.*, 2009]. Cross-shore sections of the initial and boundary values are given in the supporting information. The model was run for eight model years, and it took six model years to reach a dynamic steady state. Capturing peak upwelling season and the period where most observed data were obtained, the monthly averaged results of January from the last two years of the simulation are analyzed and discussed.

2.2. Biogeochemical Model

An ecosystem and simple nitrogen-based biogeochemical model has previously been coupled to the physical model used here [*Fennel et al.*, 2006]. To this, we added new explicit kinetic formulations approximated by Michaelis-Menten terms with a given half-saturation constants for water-column heterotrophic nitrate reduction to nitrite, denitrification coupled to oxidation of organic matter by nitrite (heterotrophic denitrification)

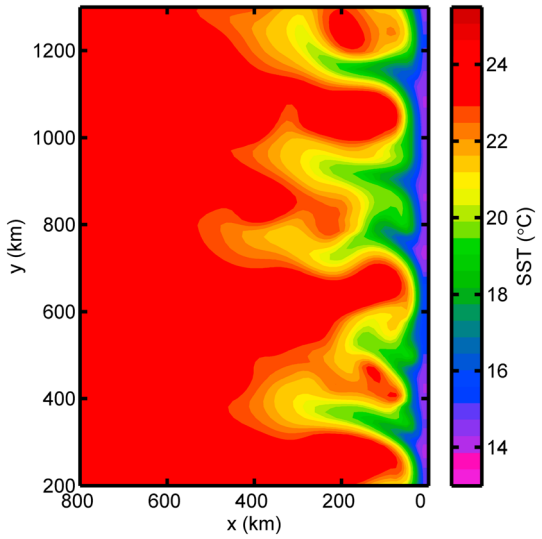

Figure 2. Model snapshot (5 days average) of simulated sea surface temperature (°C) in January shows mesoscale eddy activities of the Chilean upwelling system. As in the model, data from hydrographic stations, satellite observation, and other model studies show a relatively uniform inner coast-parallel zone of ~50 km wide with 15 – 19°C upwelled waters and ~100 km radius of mesoscale activities [*Blanco et al.*, 2001; *Thomas et al.*, 2001; *Chaigneau et al.*, 2009; *Colas et al.*, 2011].

and sulfide oxidation by nitrite (sulfide-driven denitrification), sulfate reduction, sulfide oxidation by nitrate (chemolithoautotrophic nitrate reduction) and oxygen, anammox, nitrogen fixation by nitrogen-fixing phytoplankton, and nutrient phosphate, as well as a modified formulation of bottom boundary conditions for oxic-anoxic remineralization reactions. We also modified the approximation of nitrification by resolving aerobic ammonium oxidation to nitrite and aerobic nitrite oxidation to nitrate. Here, we refer to the sum of the heterotrophic denitrification and sulfide-driven denitrification as canonical denitrification to distinguish the N_2 gas loss pathways from anammox. The kinetic formulations for the associated processes mentioned above are presented in Appendix A (i.e., equations (A5) to (A8), (A13) to (A15), (A18), and (A19)), while the half-saturation constants used in this study are listed in Table B1. The biogeochemical model consists of 14 state variables: nitrate (NO_3), nitrite (NO_2), ammonium (NH_4), phosphate (PO_4), oxygen (*Oxy*), hydrogen sulfide (H_2S), two classes of phytoplankton (phytoplankton (*Phy*) and nitrogen-fixing diazotrophs (*Diaz*)), zooplankton (*Zoo*), small and large detritus with variable nitrogen and phosphorus contents (*SDetN*, *LDetN*, *SDetP*, and *LDetP*, respectively), and chlorophyll (*Chl*). The model schematic is presented in Figure 1. In the text below, the new aspects of the biogeochemical model are briefly introduced, while Appendix A and B present all reaction equations, model parameters, and source-minus-sink terms of the state variables.

Organic matter in the water column is remineralized by different respiration processes which use various electron acceptors such as oxygen, nitrate, nitrite, and sulfate [c.f. *Canfield et al.*, 2005; *Morel and Hering*, 1993]. The availability of these electron acceptors for utilization is often considered to be based on free energy gain, so that oxic mineralization is first, followed by nitrate reduction to nitrite, then denitrification, and last by sulfate reduction (equations (A1) to (A4)). However, this sequence of events is challenged by the measured occurrence of nitrate reduction and recent recognition of sulfate reduction within the zone of nitrate reduction in the eastern tropical South Pacific OMZ [*Lipschultz et al.*, 1990; *Kalvelage et al.*, 2011; *Canfield et al.*, 2010], and is only an approximate description of the progress of these processes as seen in sediments [*Canfield*, 1993]. Therefore, in the model, the reaction rates of the remineralization pathways are regulated via Michaelis-Menten kinetic terms with a given half-saturation constant (Table B1). The constants are obtained based on direct measurements or other model values available from the literature. In this formulation, a hyperbolic function of the species concentration limits the maximum reaction rate, while one minus of the hyperbolic function inhibits other pathways. Such formulations have previously been used in sediment diagenetic models [*Van Cappellen et al.*, 1993; *Soetaert et al.*, 1996]. The oxic organic matter remineralization rate is limited by the oxygen concentration in the water column (equations ((A1) and (A5)). The rates of heterotrophic nitrate reduction to nitrite (equations (A2) and (A6)) and of heterotrophic denitrification (equations (A3) and (A7)) are both inhibited by oxygen and are limited by nitrate and nitrite, respectively. The sulfate reduction rate is inhibited by oxygen and nitrate (equations (A4) and A8) as has previously been done in sediment diagenetic modeling [*Soetaert et al.*, 1996].

In the model, a small amount of nitrite is also produced by the nitrification of ammonium in the dark and oxic environment (equation (A16)), which is further oxidized to nitrate (equation (A17)), as suggested from photoinhibition measurements for marine nitrifying bacteria by *Olson* [1981]. Ammonium is also oxidized by nitrite under anoxic condition through the anammox process to produce N_2 gas as suggested by *Kuypers et al.* [2005] and *Thamdrup et al.* [2006]. Sulfide is produced during anaerobic carbon remineralization by sulfate-

reducing bacteria. As a fast reaction, sulfide is re-oxidized back to sulfate based on the presence of oxygen, nitrate, or nitrite [*Konovalov et al*., 2006; *Jensen et al*., 2009]. We apply a two-step nitrogen-dependent sulfide oxidation path by employing oxidation by nitrate to produce some nitrite (chemolithoautotrophic nitrate reduction; equation (A10)) and oxidation by nitrite as a source for N_2 gas production (sulfide-driven denitrification; equation (A11)) [*Lam and Kuypers*, 2011]. We assume that sulfide oxidation is dominated by nitrate reduction, and not nitrite reduction, by choosing a higher half-saturation constant together with a lower first-order rate constant of nitrite reduction to N_2 relative to the chemolithoautotrophic reduction of nitrate to nitrite as described by *Jensen et al*. [2009] in the chemocline of a Danish fjord. In order to accurately simulate the observed rate of total N_2 production by *Canfield et al*. [2010], we find that it is important for the model to distinguish and quantify the relative contributions of heterotrophic nitrite reduction to N_2 and sulfide-driven nitrite reduction in the production of N_2 through canonical denitrification in the OMZ.

Explicit nitrogen-fixing diazotrophs are introduced in the model to regulate nitrogen fixation, where the growth rate depends on temperature, light, and phosphate concentration [*Fennel et al*., 2002; *Schmittner et al*., 2008]. Inclusion of this process is important for reproducing the observed primary production rates and subsequent nitrate removal in the deeper anoxic waters [cf. *Canfield*, 2006]. Liebig's law of the minimum is used to switch between the Michaelis-Menten limitation terms of nitrogen-based nutrients and phosphate, determining the growth rate of nondiazotrophic phytoplankton as implemented by *Fennel et al*. [2002] and *Schmittner et al*. [2008].

Spatially uniform vertical profiles of nitrate, phosphate, and oxygen are imposed as initial and open boundary conditions. These profiles were obtained by fitting an analytical equation to the horizontal average of the NODC World Ocean Atlas 2005 depth profiles off the northern Chilean coast (17°S to 22°S) [*Garcia et al*., 2006]. Small and homogeneous initial values of 0.1 mmol m^{-3} N, P, and H_2S were set for all other biological variables [*Fennel et al*., 2006]. A small initial value of 10^{-3} mmol m^{-3} N was set for nitrogen-fixing diazotrophs biomass in order to avoid an overestimate of the nitrogen fixation rate at the beginning of the model run. Our model constant-parameter values (Table B1) are obtained with minor tuning to the published values from observations and other model calculations [*Soetaert et al*., 1996; *Yakushev et al*., 2007; *Jensen et al*., 2009].

Two classes of organic matter (small and large detritus) are remineralized as they sink in the water column based on their rate constant of remineralization (d^{-1}) and concentrations (mmol m^{-3}). At the bottom boundary, for conservation of mass and simplicity, we assume that the fraction of sinking organic matter that is not fully remineralized in the water column is instantaneously remineralized back into the overlying water, without burial, once it reaches the seafloor. The bottom boundary calculation is less important for the present model simulation because a vertical wall is used in the eastern coastal boundary without any shallow continental shelf. However, for completeness, we present results from a biogeochemical bottom boundary condition with an extended shelf-width profile comparable to the Chile margin OMZ. The simulated ratio of organic carbon oxidation by nitrate and oxygen in the bottom water as a function of bottom water oxygen concentration is compared to the observed ratio in the sediment by *Canfield* [1993] (Appendix C, Figure C1).

3. Results

In what follows below, we first compare the simulated flow structure, averaged alongshore, with typical coastal upwelling features. Then, we verify that the simulation gives comparable model results to the available observations of the biochemical process rates and their depth distributions, as well as the depth distribution of chemical species. We focus on the monthly averaged results of January which correspond to the period where most observed data were obtained by *Canfield et al*. [2010].

3.1. Mean Circulation Structure

Due to offshore Ekman transport, upwelled water at the coast results in the typical inclined upward thermocline as seen in the alongshore-mean temperature profile of the model (Figure 3a). The upwelled water originates from the 15°C isotherm located at ~60 m depth offshore and results in a surface temperature difference of approximately 5°C from the coast to 150 km offshore. These features are consistent with the observations in the Peru-Chile upwelling system [*Blanco et al*., 2001; *Carr and Kearns*, 2003]. Mesoscale eddies and filaments arising from instabilities of the alongshore currents are generated within ~200 km from the coast as depicted from the sea surface temperature of the model (Figure 1, 3a). These mesoscale dynamics

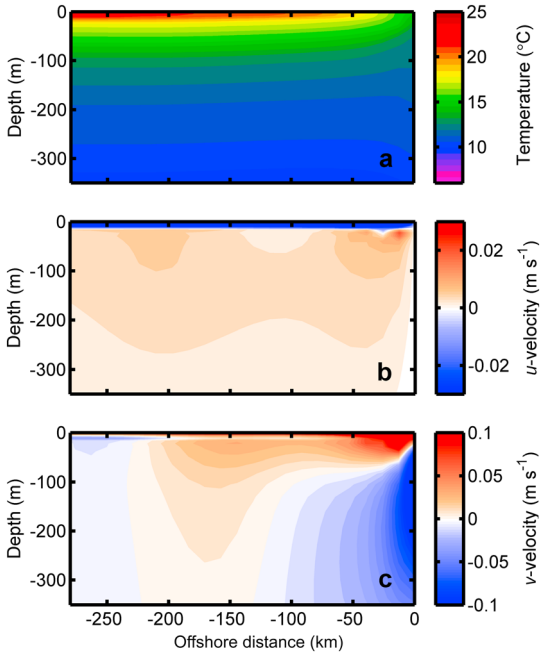

Figure 3. Model (a) temperature, (b) cross-shore velocity (negative velocities are westward), and (c) alongshore velocity field (negative velocities are southward). The results are averaged alongshore and over January in the last two years of the simulation. Note the important presence of the poleward undercurrent along the coast between 30 m and 300 m as observed by *Wooster and Gilmartin* [1961] and *Blanco et al*. [2001].

agree well with the observed data and with other model simulations of Peru-Chile upwelling [*Chaigneau et al*., 2011; *Colas et al*., 2011].

The equatorward wind forcing drives relatively constant magnitude shallow offshore Ekman transport from surface to approximately 22 m depth with an onshore compensating transport below it (Figure 3b). The common surface coastal jet reaches an equatorward velocity of 0.2 m s^{-1} due to the cross-shore pressure gradient (Figure 3c). The corresponding poleward undercurrent driven by the alongshore pressure gradient extends from above 100 m to 300 m depth. The poleward undercurrent has a maximum of 0.2 cm s^{-1} at 150 m depth, in agreement with observations in the northern Chilean upwelling system [*Wooster and Gilmartin*, 1961; *Blanco et al*., 2001].

3.2. Mean Biogeochemical Fields

The model simulation yields a good fit to the observed vertical biogeochemical concentration profiles and the measured anoxic process rate distributions by *Canfield et al*. [2010] and the 2009 cruise (Figure 4 and Table 1).

In the model, oxygen concentration reaches 212 mmol O_2 m^{-3} in the surface waters and decreases rapidly from 10 m to 80 m depth. Oxygen is consumed nearly completely (≤ 0.1 mmol O_2 m^{-3}) between 100 m and 200 m (Figure 4a). Below 300 m, the oxygen concentration slightly rises again to ~5 mmol O_2 m^{-3} as in observations.

The modeled vertical nitrate profile is in good agreement with observations (Figure 4b). The uptake of nitrate during phytoplankton growth results in the low surface nitrate concentration of 2 mmol N m^{-3}. The concentration increases to 18 mmol N m^{-3} at 65 m depth because uptake is diminished as light levels decrease but also because nitrate is produced from the nitrification of ammonium liberated during organic matter mineralization (Figure 4b). Nitrate then decreases to a minimum concentration of 10 mmol N m^{-3} at 130 m depth.

This minimum subsurface nitrate concentration represents the typical nitrate minimum as observed in oxygen-depleted OMZs (Figure 4b) and is driven by nitrate and nitrite loss to N_2 gas as explored in more detail below. The nitrate concentration increases again below 160 m to approximately 19 mmol N m^{-3} at 300 m which corresponds to the depth of increasing oxygen concentration. Nitrate concentration plotted in cross section perpendicular to the coastline shows that the high nitrate concentration at 60 m depth is upwelled to the surface near the coast with a continuous subsurface tongue of low nitrate concentration from 50 km and further offshore (Figure 5c). The minimum nitrate concentration dips to 150 m depth by 125 km offshore, where rates of organic remineralization by nitrate reduction are significantly higher than the production rates of nitrate by aerobic nitrite oxidation (Figure 5c). This result is comparable with the cruise data in 2009 which observed minimum nitrate concentration located ~120 km from the northern Chile shore at ~150 m depth. The resultant location of minimum nitrate concentration corresponds to the higher particle export between 100 and 150 km offshore (Figure 5a).

Low nitrite concentrations of less than 0.7 mmol N m^{-3} are found from the surface to 64 m depth due to high rates of nitrite oxidation by the high available oxygen concentrations (Figure 4c). A typical subsurface nitrite maximum results from high rates of ammonium oxidation from aerobic organic matter decomposition and is

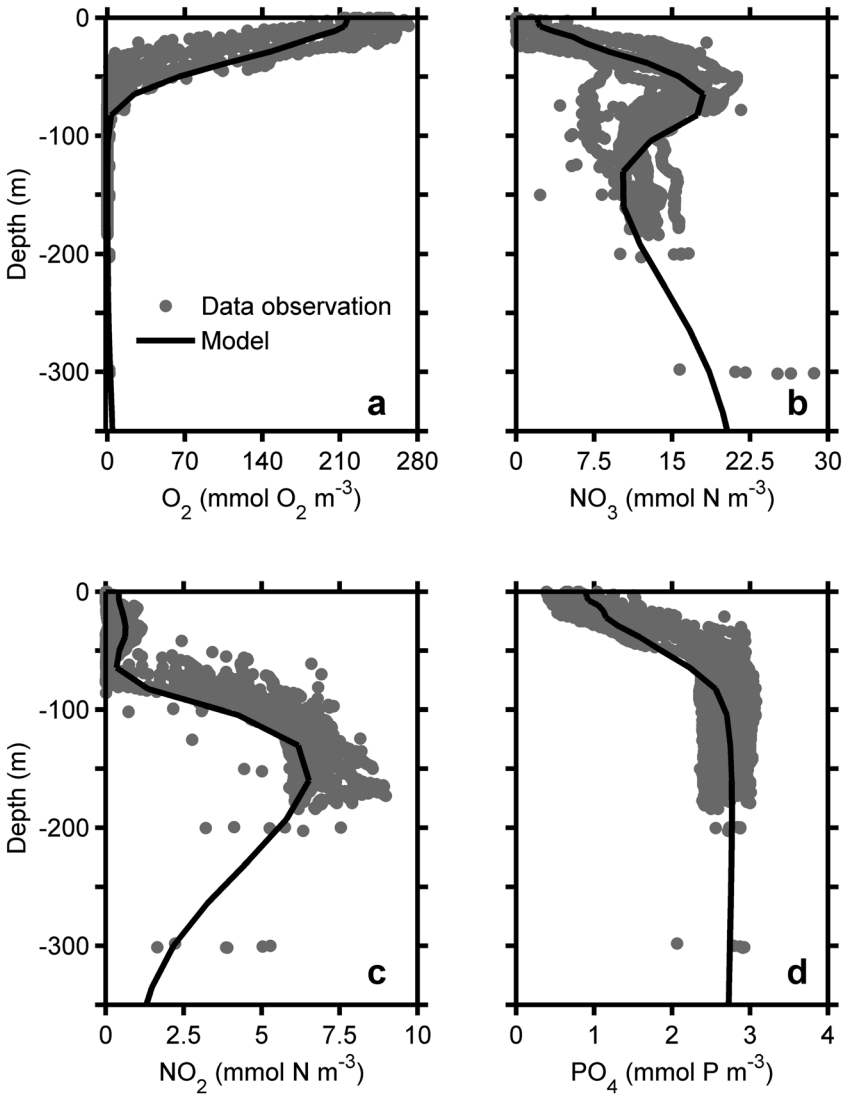

Figure 4. Modeled and observed (a) oxygen, (b) nitrate, (c) nitrite, and (d) phosphate concentration offshore Chile (~ 20°S). The solid black lines are the modeled results. The grey circles represent station data from 2009 and 2010 cruises. The results are averaged over January in the last two years of the simulation, alongshore, and from the coast to 80 km offshore. Note the reduced nitrate concentration and presence of the nitrite maximum in the oxygen-minimum depth of 100 to 200 m.

captured by the model at 30 m depth with a nitrite concentration of 0.6 mmol N m^{-3}. Deeper, from 65 m to 160 m, the nitrite concentration increases up to a maximum of 6.5 mmol N m^{-3} as a product of nitrate reduction to nitrite during organic matter remineralization in the upper portion of the low-oxygen zone. Deeper still, nitrite decreases from the depth of its maximum to a low concentration of 2.0 mmol N m^{-3} at 300 m. A band of high nitrite concentration is uniformly developed at 120 m to 200 m depth from 50 km near the coast to offshore with a maximum concentration in 125 km offshore (Figure 5d). The highest ammonium concentration of 0.78 mmol N m^{-3} is situated ~240 km offshore at 30 m water depth, whereas maximum concentrations of 0.10 to 0.65 mmol N m^{-3} are located between the coast and 150 km offshore at the same depth. Lower ammonium concentrations of 0.01 to 0.03 mmol N m^{-3} are produced at the oxygen-depleted depths between 100 and 300 m. This vertical distribution is in good agreement with observations [*Thamdrup et al.*, 2006; *Dalsgaard et al.*, 2012]. The modeled ammonium distributions perpendicular to the coast are presented in supporting information.

Finally, the vertical distribution of phosphate also agrees well with the observed data by *Canfield et al.* [2010] (Figure 4d). Phosphate levels of 0.5 mmol P m^{-3} in the surface rapidly increase to 2.7 mmol P m^{-3} at 100 m.

Table 1. Depth Integrated Process Rates of the Model With its Standard Deviation Compared to the Observed Rates

Depth Integrated Rates	Equation and Stoichiometry	Model	Observed Rate
Sulfate reduction (mmol S m^{-2} d^{-1})[a] (in ( ) as mmol C m^{-2} d^{-1})[c]	A4	0.36 ± 0.02 (0.75 ± 0.10)	0.28 – 1.00[d]
Heterotrophic denitrification (heterotrophic nitrite reduction to N_2) (mmol N m^{-2} d^{-1})[b] (in ( ) as mmol C m^{-2} d^{-1})[c]	A3	0.23 ± 0.05 (0.27 ± 0.01)	n.d.
Sulfide-driven denitrification (sulfide oxidation coupled to nitrite reduction) (mmol N m^{-2} d^{-1})[b]	A11	0.13 ± 0.02	n.d.
Canonical denitrification (heterotrophic denitrification + sulfide-driven denitrification) (mmol N m^{-2} d^{-1})	A3 + A11	0.36 ± 0.06[b]	0.10 – 0.22[b]; 1.20 – 3.80[e]
Heterotrophic nitrate reduction to nitrite (mmol N m^{-2} d^{-1})[b] (in ( ) as mmol C m^{-2} d^{-1})[c]	A2	3.21 ± 0.54 (0.97 ± 0.05)	4.70 – 9.90[f]
Total organic C remineralization (mmol C m^{-2} d^{-1})[c]	A1 to A4	2.08 ± 0.22	1.00 – 2.50[g]
Anammox (mmol N m^{-2} d^{-1})	A20	0.53 ± 0.05[b]	0.70 – 1.21[b,d]; 0.14[h]
Primary productivity (g C m^{-2} d^{-1})		3.13	2.00 – 3.50[i]
Surface nitrogen fixation (μmol N m^{-2} d^{-1})		16.19	7.5 – 190[j]

[a] Integrated from 85 to 150 m.
[b] From 73.5 to 173 m for comparison with *Canfield et al.* [2010].
[c] Integrated from 100 to 170 m for internal model comparison.
[d] *Canfield et al.* [2010].
[e] Estimated from *Dalsgaard et al.* [2012] for observations at ~14°S (integrated from 75 to 150 m) and ~26°S (integrated from 90 to 150 m) in February 2007.
[f] Estimated from Peruvian OMZ [*Lam et al.*, 2009].
[g] Estimated from *Escribano et al.* [2004].
[h] Estimated from *Dalsgaard et al.* [2012] for observations at ~20°S (integrated from 50 to 100 m) in February 2007.
[i] *Carr and Kearns* [2003].
[j] *Fernandez et al.* [2011].
n.d.: no data.

Deeper than 110 m, phosphate has a constant concentration of 2.7 mmol P m^{-3} in agreement with the mean observed profile. Nutrient chemistry of the model shows a nitrogen deficit in the Chile OMZ as indicated by a deviation from the Redfield N/P ratio into a ratio lower than 16, in agreement with the observed N/P ratio (Figure B1). Additionally, the modeled N-deficit calculated as $[NO_3] + [NO_2] - 16 \times [PO_4]$ extends from -25 to -28 mmol m^{-3} in 100 to 170 m water depth of the OMZ. This modeled N-deficit is comparable with measurement by *Altabet et al.* [2012] in the southern Peru OMZ at the same depth range (Figure B2). Thus, nitrogen is limiting in the Chile OMZ system.

3.3. Anoxic Process Rates

The dynamic coupling between the nitrogen and sulfur cycles is modeled here for the first time in a three-dimensional ocean model of a coastal upwelling system. Depth-integrated rates of heterotrophic nitrate reduction to nitrite, sulfate reduction, heterotrophic denitrification, chemolithoautotrophic nitrate reduction, sulfide-driven denitrification, anammox, and corresponding rates of nitrogen fixation and primary productivity for the conducted simulation are compared with the observed rates, where available, in Table 1. In the model, the depth-integrated rate of heterotrophic nitrate reduction is the most dominant pathway of organic carbon remineralized under anoxic conditions. An important role for this process in carbon mineralization was suggested earlier in these waters by *Thamdrup et al.* [2006] and documented in more recent experimental work off the Peruvian coast by *Lam et al.* [2009]. Our model also shows that rates of carbon mineralization by sulfate reduction exceed rates of carbon mineralization through nitrite reduction to N_2, again in agreement with observations (Table 1). It is noteworthy that our results were obtained by tuning of various model and measured parameter constants (Table B1).

The anoxic process rates are reproduced in the simulation where we assume that chemolithoautotrophic nitrate reduction (sulfide oxidation by nitrate) dominates over sulfide-driven denitrification (sulfide oxidation by nitrite) [*Jensen et al.*, 2009] (Table B1). This assumption may be subject to revision in future studies as we have only limited understanding on how this nitrogen-dependent sulfide oxidation is regulated in OMZs, other than the fact that the observed rate of heterotrophic nitrate reduction (to nitrite) is higher than the heterotrophic denitrification rate.

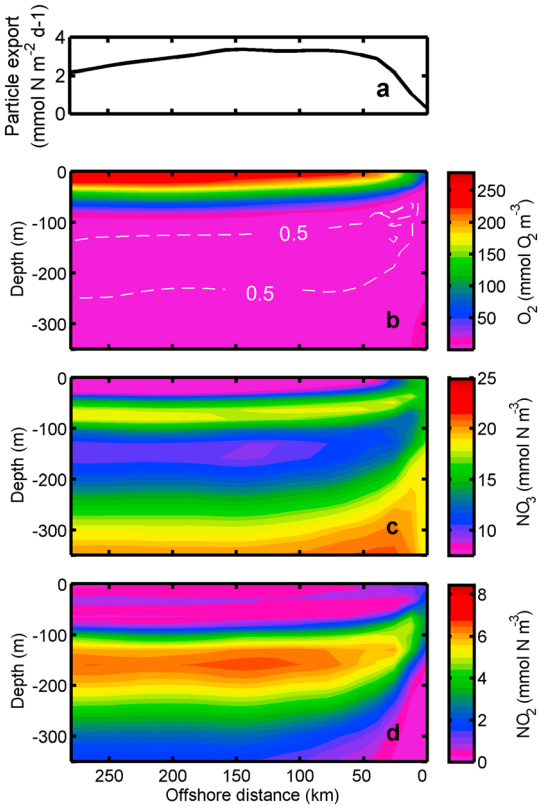

Figure 5. Model transects perpendicular to the coast. (a) Export of particulate organic matter at 50 m depth and biogeochemical fields of (b) oxygen, (c) nitrate, and (d) nitrite concentration. The results are averaged alongshore and over January in the last two years of the simulation. Importantly, extensive anaerobic remineralizations implied by reduced nitrate and maximum nitrite concentration occurred in 100–150 km from the coast at the depth of 100–200 m. Those high remineralizations correspond to the higher organic particle export at 50 to 150 km offshore.

The modeled rate of sulfate reduction is within the wide observed range, while the rate of canonical denitrification (heterotrophic denitrification plus sulfide-driven denitrification) exceeds the range of observed rates at this latitude (Table 1). The observed rates represent snapshots from only two stations located 22 and 68 km off shore, respectively, and indicate a pronounced yet poorly resolved zonal gradient [*Canfield et al*., 2010; *De Brabandere et al*., 2013], while the modeled rate represents a 1 month and spatial average along shore and 0–80 km offshore. We further note that higher canonical denitrification rates have been sporadically observed at different depths along Peruvian and Chilean coasts in February 2007, and it was suggested that experimental denitrification rates may be biased towards underestimation due to undersampling of activity hot spots possibly associated with sinking aggregates [*Dalsgaard et al*., 2012]. Furthermore, the higher rate as suggested here may be indirectly supported by the observation that denitrifying bacteria are quite abundant in OMZs, even when their activities are low, perhaps because of their living modes and dormancy [*Ward et al*., 2007; *Lam and Kuypers*, 2011]. Hence, we would argue that rate of canonical denitrification as produced in the model may be comparable to the real world despite being higher than some of the current observations.

The simulation result underestimates the anammox rate by 24% – 43% compared to the rates observed by *Canfield et al*. [2010]. Similar to the canonical denitrification, this may reflect the fundamental differences between the top-down and bottom-up approaches of modeling and experiments, respectively. This underestimate may also be due to our model generates nitrite concentrations at the lower end of the field observations (Figure 4). However, the modeled rate is higher compared to observations at ~20°S off Chile's coast by *Dalsgaard et al*. [2012] during a cruise in February 2007 (Table 1). Alternatively, an underestimation of anammox and overestimation of denitrification by the model could potentially arise if dissimilatory nitrite reduction to ammonium (DNRA) contributed to carbon oxidation and sulfide reoxidation, and the resulting production of ammonium was coupled to anammox [*Lam et al*., 2009]. However, DNRA was not detected at 20°S in January 2010 [*De Brabandere et al*., 2013], which argues against this explanation and justifies that DNRA was not included in the model.

Simulated rates of nitrogen fixation, integrated from the surface to 120 m, from growth of N_2-fixing phytoplankton, are within the observed rates by *Fernandez et al*. [2011] at the same depth range which suggests some input of fixed-nitrogen source in the Chilean OMZ (Table 1). The model only resolves nitrogen fixation in surface waters assuming that the growth of N_2-fixer phytoplankton depends on the availability of light in addition to the specifics of temperature and phosphate concentration (equation (B12)) [*Fennel et al*., 2002; *Schmittner et al*., 2008]. A recent study has shown that substantial N_2 fixation may also at times take

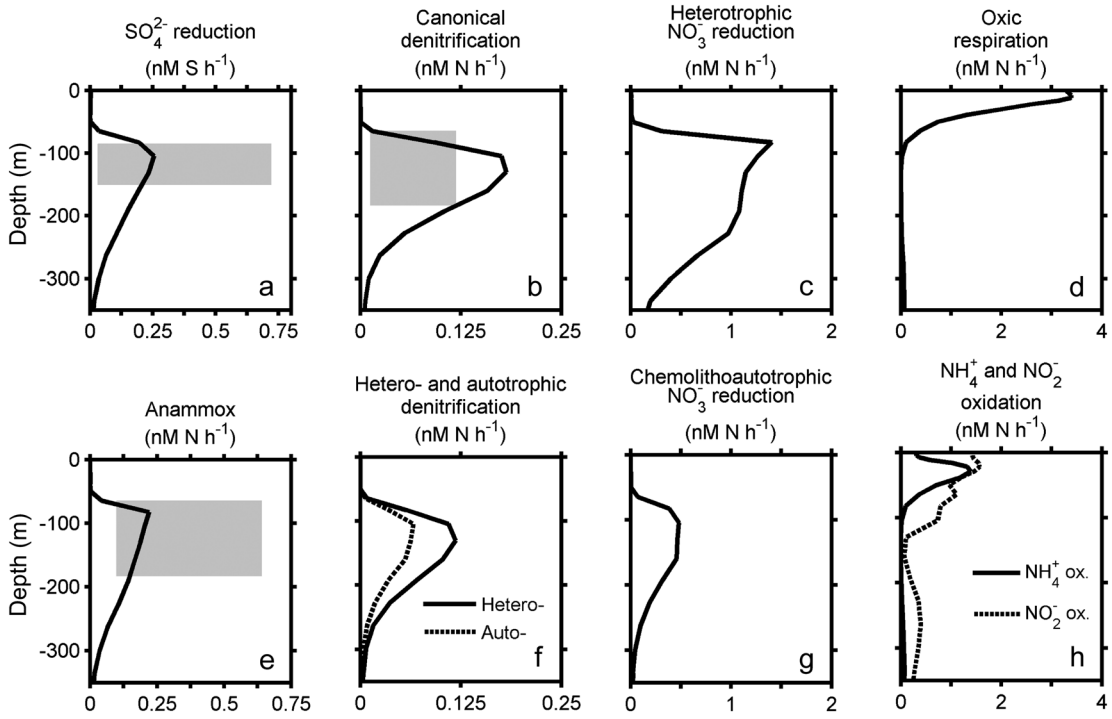

Figure 6. Modeled vertical distribution of (a) sulfate reduction rate, (b) canonical denitrification rate, (c) heterotrophic NO_3 reduction rate, (d) oxic remineralization rate of organic matter, (e) anammox rate, (f) heterotrophic (solid line) and sulfide-driven denitrification rates (dashed line; sulfide oxidation rate by NO_2), (g) chemolithoautotrophic NO_3 reduction rate (sulfide oxidation rate by NO_3), and (h) NH_4 (solid line) and NO_2 (dashed line) oxidation rate by O_2. The model results are averaged alongshore, over January in the last two years of the simulation, and from the coast to 80 km offshore. Grey areas indicate the range of the available observed rates from *Canfield et al.* [2010]. Note the different scales used for the rates in these plots. Heterotrophic NO_3 reduction is the most dominant pathway for the anaerobic remineralizations in the model, followed by sulfate reduction and heterotrophic denitrification. The modeled anammox rate is more important than the canonical denitrification rate (sum of heterotrophic and sulfide-driven denitrification rates) in releasing N_2 gas.

place in the dark OMZ core [*Fernandez et al.*, 2011]. While this challenges fundamental concepts about N cycling in OMZs, the lacking understanding of the temporal and spatial variations of this fixed nitrogen source precludes realistic modeling. The modeled rate of nitrogen fixation corresponds to approximately 2% of nitrogen-loss rate through the combination of canonical denitrification and anammox (Table 1).

The time and alongshore-averaged process rates in the model are presented in Figure 6 to show the depth distributions of the coupled sulfur and nitrogen processes. Sulfate reduction exhibits its maximum rate at approximately 100 m depth, whereas the maximum rate of heterotrophic denitrification to N_2 is somewhat shallower and heterotrophic nitrate reduction to nitrite and anammox is slightly shallower again. The depth profiles of the sulfide-driven nitrate and nitrite reduction correspond to the sulfate reduction rate profile, while the nitrification of ammonium and nitrite have profiles correlating with the oxic respiration rate profile. The rates of heterotrophic metabolism decrease considerably below 300 m water depth because most labile organic matter has been remineralized. The alongshore-averaged vertical section of the sulfate reduction rate shows that the maximum rate is located between 100 and 150 km from the coast and decreases uniformly further offshore in this model configuration (Figure 7).

The depth-integrated (100 to 170 m) summary of modeled nitrite and ammonium sources and sinks are listed in Table 2, with rates integrated from near the coastal boundary to 200 km offshore. There is a net balance in the ammonium sources and sinks. Anammox accounts for 97% of the ammonium sink, and the ammonium driving anammox is supplied 48% from heterotrophic nitrate reduction to nitrite, 35% from sulfate reduction, and 17% from heterotrophic denitrification. There is net production of nitrite in the OMZ depths, where the greatest source is from heterotrophic nitrate reduction while the major sink is nitrite oxidation by oxygen at the chemocline (Table 2). A nitrite maximum is a typical feature of OMZs, while anammox and nitrification with oxygen will be important sinks for nitrite in the very low oxygen waters of the OMZs [*Codispoti et al.*, 1986; *Ward et al.*, 1989; *Thamdrup et al.*, 2006]. Processes controlling sulfide oxidation exhibit an essential role

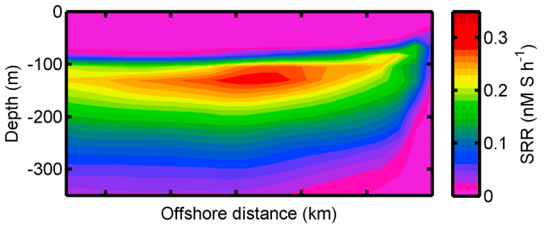

Figure 7. Vertical section of the modeled sulfate reduction rate. The plot is averaged alongshore and over January in the last two years of the simulation. Note that the higher sulfate reduction rate at 100 – 150 km from the coast corresponds to the maximum export production at approximately the same distance offshore (50–150 km). There is no sulfate reduction rate occurrence above ~100 m and below ~350 m depth because of the presence of oxygen.

in the regulation of nitrite production and loss. Approximately 28% of nitrite production is contributed by chemolithoautotrophic sulfide oxidation coupled to nitrate reduction, while 15% of nitrite loss into gaseous N_2 is caused by the sulfide oxidation coupled to nitrite reduction (Table 2). Anammox also plays an important role in nitrite removal, contributing 23% of the total nitrite loss, in agreement with measurements (*Thamdrup et al.* [2006]) (Table 2).

4. Discussion and Conclusions

A recently observed cryptic sulfur cycle in the oxygen-minimum zone (OMZ) of the Chilean upwelling system is believed to be coupled to nitrogen cycling, potentially influencing other oceanic biogeochemical cycles [*Canfield et al.*, 2010]. Our approach here is to assess the dynamic coupling between the nitrogen, sulfur, and oxygen cycles using a three-dimensional coupled circulation and biogeochemical ocean model in the Chile OMZ. The coupled model has extensive modifications to the nitrogen-based ecosystem model by *Fennel et al.* [2006] making it applicable to anoxic systems. The developed module includes heterotrophic nitrate reduction to nitrite, heterotrophic nitrite reduction to N_2 (heterotrophic denitrification), sulfate reduction, sulfide oxidation by oxygen, nitrite and nitrate, aerobic nitrification of ammonium and nitrite, anammox, as well as an implementation of nitrogen fixation by N_2-fixing phytoplankton. The model reproduces well the distribution of chemical species process rates within the Chilean OMZ system.

Our model indicates that sulfate reduction contributes a significant portion of total organic carbon remineralization in the Chile OMZ. The modeled sulfate reduction provides 36% of the total organic carbon remineralization below the mixed layer to a depth of 150 m, whereas the highest contribution of 47% comes from heterotrophic nitrate reduction to nitrite and only 13% by heterotrophic denitrification (Table 1). These results demonstrate that a very active cryptic sulfur cycle in the OMZ of Chilean upwelling systems as observed by *Canfield et al.* [2010] can be simulated with realistic parameters. A similar sulfur cycle may also be present in other OMZs waters but direct observations are currently lacking. We believe, however, that the model developed in this study has potential applications to other oxygen-depleted waters because model parameters are changed little relative to those diagnosed from chemostat experiments and other related modeling investigations [*Soetaert et al.*, 1996; *Yakushev et al.*, 2007; *Thamdrup et al.*, 2012]. For example, the model development and analysis here could become an important transition point to model and investigate free-sulfide

Table 2. Depth Integrated NO_2 and NH_4 Sources and Sinks From 100 to 170 m in the Unit of mmol N m^{-2} d^{-1} With its Standard Deviation

NO_2 and NH_4 Sources and Sinks	Rate of the Model
NO_2 sources	
NH_4 oxidation by O_2	0.01 ± 0.01
Heterotrophic NO_3 reduction	1.95 ± 0.09
Chemolithoautotrophic NO_3 reduction[a]	0.77 ± 0.02
Total	2.73 ± 0.12
NO_2 sinks	
NO_2 oxidation by O_2	0.43 ± 0.30
Heterotrophic denitrification	0.36 ± 0.02
Sulfide-driven denitrification[b]	0.20 ± 0.01
Anammox	0.30 ± 0.02
Total	1.29 ± 0.35
NH_4 sources	
O_2 respiration in organic remineralization	0.01 ± 0.01
Heterotrophic denitrification	0.04 ± 0.01
Heterotrophic NO_3 reduction	0.15 ± 0.01
SO_4 reduction	0.11 ± 0.01
Total	0.31 ± 0.04
NH_4 sinks	
NH_4 oxidation by O_2	0.01 ± 0.01
Anammox	0.30 ± 0.02
Total	0.31 ± 0.03

[a] H_2S oxidation by nitrate.
[b] H_2S oxidation by nitrite.

occurrence as occasionally observed in the continental shelf bottom waters of the Namibian coastal upwelling system [*Bruchert et al*., 2003 and *Lavik et al*., 2009].

Our model analysis suggests a strong coupling between the nitrogen and sulfur cycles in the Chilean OMZ, not only because the depleted oxygen and low nitrate water column allow sulfate reduction, but also because the sulfide oxidation removes a fixed amount of nitrogen. In our simulation, sulfide is oxidized mostly by nitrate, whereas the oxidation by nitrite reduction contributes to a removal rate of fixed nitrogen to N_2 gas, which is approximately 36% of the canonical denitrification rate. To our knowledge, the uncoupling between heterotrophic denitrification and sulfide-driven denitrification has not been addressed in any other models. Thus, the model presented here provides the first insight as to how those two processes contribute to N_2 loss in OMZ settings. The model substantiates that anammox is the dominant N_2 production process, consistent with observation by *Thamdrup et al*. [2006], and shows that both heterotrophic nitrate reduction to nitrite and sulfate reduction are the most important sources of ammonium for anammox in OMZ depths.

Modeled nitrogen fixation by N_2-fixing phytoplankton supplies additional nitrogen-based nutrients (ammonium and nitrate) in surface layers, in agreement with the range of integrated nitrogen fixation rates observed from surface to 120 m depth by *Fernandez et al*. [2011] in the Chile-Peru OMZ. Recent finding of high nitrogen fixation activity in the subsurface oxygen depths measured by *Fernandez et al*. [2011] was unresolved in this study due to the simple and robust approximation of the growth of N_2-fixing phytoplankton used in the model. Further development of the model based on spatially and temporarily more reliable observations and better understanding of how and which N_2-fixing plankton is present in the aphotic subsurface depths are needed. The nitrogen fixation of the model, however, is not expected to fully satisfy the nitrogen deficit in OMZ depths, as implied by the lower N (nitrate + nitrite) to P (phosphate) ratio compared to the Redfield ratio (Figure B1). It has been suggested that a full compensation of the nitrogen deficit by nitrogen fixation would totally deplete the nitrate concentration and create water column sulfidic condition because greater nitrogen fixation generates higher production of sinking organic matter being remineralized by nitrate reduction and followed by sulfate reduction [*Shaffer*, 1989; *Canfield*, 2006]. Therefore, in order to maintain the observed persistence of nitrate, it is more realistic that the nitrogen fixation of the model only partially amends the nitrate deficit.

Appendix A: Equation of the Water Column Remineralization and Anoxic Reaction

The nitrogen-based biogeochemical model of *Fennel et al*. [2006] is modified to handle oxic and anoxic remineralization, ammonium and nitrite oxidation, sulfide oxidation, and anammox. In this section, we describe the reactions and equation that were added and modified. The complete source and sink terms of all biogeochemical variables are presented in Appendix B.

Organic matter remineralization in the water column of the model is regulated by a sequence of oxidant availability which is oxygen, nitrate, and nitrite. Depending on the oxidant concentrations, the remineralization pathways are, in sequence, oxic remineralization, coupled heterotrophic nitrate reduction and denitrification, and sulfate reduction. When oxygen is limiting, the organic matter is degraded by oxic remineralization following *Lipschultz et al*. [1990]:

$$(CH_2O)_{106}(NH_3)_{16}H_3PO_4 + 106O_2 \rightarrow 106CO_2 + 16NH_3 + H_2PO_4 + 122H_2O \quad \text{(A1)}$$

Subsequently, when nitrate and nitrite are limiting and oxygen is inhibiting, we apply a coupled heterotrophic nitrate reduction (equation (A2)) and denitrification (equation (A3)) based on *Anderson et al*. [1982]. First, the remineralization consumes nitrate to produce nitrite (heterotrophic nitrate reduction):

$$\frac{1}{2}\left[(CH_2O)_{106}(NH_3)_{16}H_3PO_4\right] + 106NO_3^- \rightarrow 106NO_2^- + 53H_2O + 53CO_2 + 8NH_3 + \frac{1}{2}H_3PO_4 \quad \text{(A2)}$$

and then some part of the nitrite is utilized to produce N_2 gas (heterotrophic denitrification):

$$\frac{3}{4}\left[(CH_2O)_{106}(NH_3)_{16}H_3PO_4\right] + 106H^+ + 106NO_2^- \rightarrow 53N_2 + 132.5H_2O + 79.5CO_2 + 12NH_3 + \frac{3}{4}H_3PO_4 \quad \text{(A3)}$$

Finally, sulfate is used to remineralize the organic matter when none of the other oxidants are limiting, but it is inhibited by oxygen and nitrate. The sulfate reduction reaction follows *Jørgensen* [1996]:

$$(CH_2O)_{106}(NH_3)_{16}H_3PO_4 + 53H_2SO_4 + 11H^+ \rightarrow 106CO_2 + 53H_2S + 16NH_4 + H_2PO_4 + 106H_2O \quad \text{(A4)}$$

In the model, we use a kinetic approximation to regulate the different remineralization pathways. The relative contributions of the different pathways are approximated by the Michaelis-Menten type limitation and/or inhibition formulation with a half-saturation constant. The contributions from oxic remineralization, heterotrophic nitrate reduction, heterotrophic denitrification, and sulfate reduction are represented by *oxr*, *nrr*, *dfr*, and *srr*, respectively:

$$oxr = \frac{O_2}{kO_{2\_ox} + O_2} \quad \text{(A5)}$$

$$nrr = \frac{NO_3}{kNO_{3\_an} + NO_3} \cdot \frac{kinhO_{2\_df}}{kinhO_{2\_df} + O_2} \quad \text{(A6)}$$

$$dfr = \frac{NO_2}{kNO_{2\_an} + NO_2} \cdot \frac{kinhO_{2\_df}}{kinhO_{2\_df} + O_2} \quad \text{(A7)}$$

$$srr = \frac{kinhO_{2\_an}}{kinhO_{2\_an} + O_2} \cdot \frac{kinhNO_{3\_an}}{kinhNO_{3\_an} + NO_3} \quad \text{(A8)}$$

with $sumlim = oxr + nrr + dfr + srr$ as the total contributions term. Complete description of the parameters and values is listed in Table B1. See equations (B2), (B3), (), and (B9) for the sink and source terms by the organic matter remineralization.

Sulfide, the product of sulfate reduction, is oxidized rapidly by oxygen and nitrate [*Canfield et al*., 2005]. The reaction of sulfide oxidation by oxygen follows *Konovalov et al*. [2006]:

$$H_2S + 2O_2 \rightarrow 2H^+ + SO_4^{2-} \quad \text{(A9)}$$

We decouple sulfide oxidation by nitrate to N_2 gas in equation (A12) into sulfide oxidation by nitrate to nitrite (chemolithoautotrophic nitrate reduction; equation (A10)) and sulfide oxidation by nitrite to N_2 gas (sulfide-driven denitrification; equation (A11)) following reactions described by *Canfield et al*. [2010] and *Mahmood et al*. [2007]:

$$2H_2S + 8NO_3^- \rightarrow 8NO_2^- + 2SO_4^{2-} + 4H^+ \quad \text{(A10)}$$

$$3H_2S + 8NO_2^- + 2H^+ \rightarrow 4N_2 + 3SO_4^{2-} + 4H_2O \quad \text{(A11)}$$

Sum (A10) and (A11):

$$5H_2S + 8NO_3^- \rightarrow 4N_2 + 5SO_4^{2-} + 4H_2O + 2H^+ \quad \text{(A12)}$$

The model uses a Michaelis-Menten kinetic for the sulfide oxidation rate by oxygen as follow:

$$SoxO_2 = K_{SO} \cdot H_2S \cdot \frac{O_2}{kO_{2\_SO} + O_2} \quad \text{(A13)}$$

We modify a kinetic rate described by *Jensen et al*. [2009] by adding an inhibition term by oxygen for sulfide oxidation rate by nitrate and nitrite as follow, respectively:

$$SoxNO_3 = K_{SN1} \cdot H_2S \cdot \frac{NO_3}{kNO_{3\_SN} + NO_3} \cdot \frac{kinhO_{2\_SN}}{kinhO_{2\_SN} + O_2} \quad \text{(A14)}$$

$$SoxNO_2 = K_{SN2} \cdot H_2S \cdot \frac{NO_2}{kNO_{2\_SN} + NO_2} \cdot \frac{kinhO_{2\_SN}}{kinhO_{2\_SN} + O_2} \quad \text{(A15)}$$

K_{SO}, K_{SN1}, and K_{SN2} are specific rate constants of sulfide oxidation by oxygen, nitrate, and nitrite, respectively.

Table B1. List of Biochemical Parameters and Values Used in the Model

Symbol	Parameter	Value	Unit	Literature (range)
$kO2\_ox$	half-saturation concentration of O_2 in oxic mineralization	0.3	mmol O m^{-3}	0.1[a] – 15[c]
$kNO3\_an$	half-saturation concentration of NO_3 in nitrate reduction	15	mmol N m^{-3}	1[c] – 30[b]
$kNO2\_an$	half-saturation concentration of NO_2 in denitrification	30	mmol N m^{-3}	1[c] – 30[b]
$kinhO2\_df$	half-saturation concentration of O_2 inhibition in nitrate reduction and denitrification	0.1	mmol O m^{-3}	0.1[a] – 10[b]
$kinhO2\_an$	half-saturation concentration of O_2 inhibition in sulfate reduction	0.1	mmol O m^{-3}	0.1[a] – 5[b]
$kinhNO3\_an$	half-saturation concentration of NO_3 inhibition in sulfate reduction	4	mmol N m^{-3}	1 – 5[b]
K_{SN1}	constant rate of sulfide oxidation by NO_3	0.93	d^{-1}	0.93[d]
K_{SN2}	constant rate of sulfide oxidation by NO_2	0.33	d^{-1}	0.0 – 0.93[d]
K_{SO}	constant rate of sulfide oxidation by O_2	0.93	d^{-1}	0.93 – 1.90[d]
$kO2\_SO$	half-saturation concentration of O_2 in sulfide oxidation	1	mmol O m^{-3}	1[c]
$kNO3\_SN$	half-saturation concentration of NO_3 in sulfide oxidation	2.9	mmol N m^{-3}	2.9[d]
$kNO2\_SN$	half-saturation concentration of NO_2 in sulfide oxidation	6	mmol N m^{-3}	2.9 – 15[d]
$kinhO2\_SN$	half-saturation concentration of O_2 inhibition in sulfide oxidation	0.1	mmol O m^{-3}	0.1[a]
K_{MX}	constant rate of anammox rate	0.07	d^{-1} (mmol N m^{-3})$^{-1}$	0.03 – 0.1[c]
$n1_{max}$	maximum rate of aerobic ammonium oxidation	0.1	d^{-1}	0.02 – 2[e]
$n2_{max}$	maximum rate of aerobic nitrite oxidation	0.1	d^{-1}	0.02 – 2[e]
$kO2\_nit$	half-saturation concentration of O_2 in nitrification	1	mmol N m^{-3}	1 – 3[f]
$I_{th}NH_4$	radiation inhibition threshold of ammonium	0.0095	W m^{-2}	0.0095[g]
$I_{th}NO_2$	radiation inhibition threshold of nitrite	0.0364	W m^{-2}	0.0364[g]
$k_{I_NH_4}$	light intensity at which inhibition is half-saturated for ammonium	0.036	W m^{-2}	0.036[g]
$k_{I_NO_2}$	light intensity at which inhibition is half-saturated for nitrite	0.074	W m^{-2}	0.074[g]
r_{SD}	remineralization rate of suspended detritus	0.03	d^{-1}	0.03[f]
r_{LD}	remineralization rate of larger detritus	0.02	d^{-1}	0.02[f]
μ_{0P}	phytoplankton growth rate at 0°C	0.69	d^{-1}	0.69[f]
μ_{0D}	diazotroph growth rate at 0°C	0.085	d^{-1}	0.006 – 0.88[h]
θ_{max}	chlorophyll to phytoplanktonic maximum ratio	0.053	mgChl mgC^{-1}	0.053[f]
α	initial slope of planktonic growth to light curve	0.025	(W m^{-2})$^{-1}$ d^{-1}	0.025[f]
k_{NO_3}	half-saturation concentration for uptake of NO_3 by phytoplankton	0.5	mmol N m^{-3}	0.5[f]
k_{NH_4}	half-saturation concentration for uptake of NH_4 by phytoplankton	0.5	mmol N m^{-3}	0.5[f]
$R1_{P:N}$	stoichiometry of P to N in phytoplankton and zooplankton	1/16	dimensionless	1/16[i]
$R2_{P:N}$	stoichiometry of P to N in diazotroph	1/45	dimensionless	1/45[i]
k_{PO4_Phy}	half-saturation concentration for uptake of PO_4 by phytoplankton (k_{NO_3}/16)	0.03125	mmol P m^{-3}	0.03125[j]
k_{PO4_Diaz}	half-saturation concentration for uptake of PO_4 by diazotroph (k_{NO_3}/16)	0.03125	mmol P m^{-3}	0.03125[j]
l_{BM}	excretion rate due to basal metabolism	0.1	d^{-1}	0.1[f]
l_E	excretion rate due to phytoplankton assimilation	0.1	d^{-1}	0.1[f]
β	assimilation efficiency	0.75	dimensionless	0.75[f]
$g_{max\,P}$	maximum phytoplankton grazing rate	0.6	(mmol N m^{-3})$^{-1}$ d^{-1}	0.6[f]
$g_{max\,D}$	maximum diazotroph grazing rate	0.5	(mmol N m^{-3})$^{-1}$ d^{-1}	0.5[k]
m_P	phytoplankton mortality	0.15	d^{-1}	0.15[f]
m_D	diazotroph mortality	0.05	d^{-1}	0.025[j] – 0.5[k]
m_Z	zooplankton mortality	0.025	d^{-1}	0.025[f]
k_P	half saturation of phytoplankton ingestion	2	(mmol N m^{-3})$^{-2}$	2[f]
τ	aggregation parameter	0.005	d^{-1}	0.005[f]
w_P	sinking velocity of phytoplankton and diazotroph	0.1	m d^{-1}	0.1[f]
w_S	sinking velocity of small detritus	1	m d^{-1}	0.1[f] – 1[l]
w_L	sinking velocity of large detritus	8	m d^{-1}	1[f] –10[l]

[a] *Thamdrup et al.* [2012].
[b] *Soetaert et al.* [1996].
[c] *Yakushev et al.* [2007].
[d] *Jensen et al.* [2009].
[e] *Yool et al.* [2007].
[f] *Fennel et al.* [2006].
[g] *Olson* [1981].
[h] *LaRoche and Breitbarth* [2005].
[i] *Fennel et al.* [2002].
[j] *Schmittner et al.* [2008].
[k] *Monteiro and Follows* [2009].
[l] *Gruber et al.* [2006].

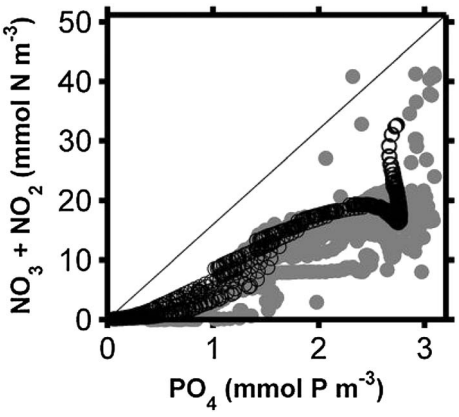

Figure B1. Ratio of nitrogen to phosphate for the model results (black open circles) compared to the ratio of the observed data (grey filled circles). The Redfield ratio is shown by the solid line. The model results are averaged over January in the last two years of the simulation, alongshore, and from the coast to 80 km offshore. Note that total fixed nitrogen of the model is not quite as reduced as in observations relative to the phosphate concentration. This shortcoming in drawdown of fixed nitrogen most likely related to the model productivity being slightly less than the observation.

The nitrification has been modified to include ammonium oxidation (referred as nitrification1, equation (A16)) and nitrite oxidation (nitrification2, equation (A17)) to produce nitrate as the end product. The nitrification only occurs under low light and aerobic condition [*Olson*, 1981].

$$NH_4^+ + 1.5O_2 \rightarrow NO_2^- + H_2O + 2H^+ \quad \text{(A16)}$$

$$NO_2^- + 0.5O_2 \rightarrow NO_3^- \quad \text{(A17)}$$

Following *Olson* [1981] and *Fennel et al.* [2006], the rate of nitrification1 ($n1$) and nitrification2 ($n2$) is determined by:

$$n1 = n1_{\max} \cdot \frac{O_2}{KO_{2\_nit} + O_2} \cdot \left(1 - \max\left(0, \frac{I - I_{th}NH_4}{k_{I\_NH_4} + I - I_{th}NH_4}\right)\right) \quad \text{(A18)}$$

$$n2 = n2_{\max} \cdot \frac{O_2}{KO_{2\_nit} + O_2} \cdot \left(1 - \max\left(0, \frac{I - I_{th}NO_2}{k_{I\_NO_2} + I - I_{th}NO_2}\right)\right) \quad \text{(A19)}$$

where $n1_{\max}$ and $n2_{\max}$ are the maximum rate of ammonium and nitrite oxidation, respectively. I is the photosynthetically available radiation, $I_{th}NH_4$ and $I_{th}NO_2$ are the radiation inhibition threshold of ammonium and nitrite, and KO_{2_nit} is the aerobic half-saturation for nitrification. $k_{I\_NH_4}$ and $k_{I\_NO_2}$ are the light intensity at which inhibition is half-saturated for ammonium and nitrite, respectively.

Under anoxic condition, ammonium is oxidized by nitrite through anammox to produce N_2 gas as described by *Thamdrup et al.* [2006]:

$$16NH_4^+ + 16NO_2^- \rightarrow 16N_2 + 32H_2O \quad \text{(A20)}$$

The kinetic of the anammox is determined by $K_{MX} \cdot NH_4 \cdot NO_2$ as implemented by *Yakushev et al.* [2007] and inhibited by $\frac{kinhO_{2\_df}}{kinhO_{2\_df}+O_2}$ as in denitrification. K_{MX} is the specific constant rate of the anammox and $kinhO_{2\_df}$ is the half-saturation concentration for oxygen inhibition.

Appendix B: Source and Sink Terms of the Biogeochemical State Variables

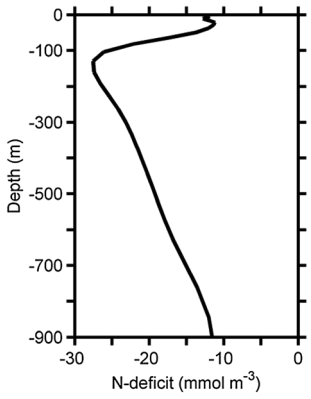

Figure B2. Modeled N-deficit calculated as $[NO_3] + [NO_2] - 16 \times [PO_4]$. The model result is averaged over January in the last two years of the simulation, alongshore, and from the coast to 80 km offshore.

The evolution of each biogeochemical concentration (C) is described by the tracer conservation equation as follow:

$$\frac{\partial C}{\partial t} = -\nabla(uC) + diff(C) + sms(C) \quad \text{(B1)}$$

where the time rate of change of C depends on water transport by three-dimensional advection (u) and diffusion ($diff$), and source and sink terms (sms) due to biological and chemical reaction. Complete descriptions of u and $diff$ terms are given by [*Shchepetkin and McWilliams*, 2005, *Haidvogel et al.*, 2008] and also can be found in www.myroms.org. Each of the biogeochemical source

and sink terms is described in the equations below.

Nitrate source and sink terms:

$$\begin{aligned} sms(NO_3) &= -\text{uptake by phytoplankton} + \text{nitrification2} \\ &\quad -\text{denitrification1} \\ &\quad -\text{chemolitoautotrophic nitrate reduction} \\ sms(NO_3) &= -\mu_{\max}\cdot L_L\cdot L_{NO_3}\cdot Phy + n2\cdot NO_2 \\ &\quad -\frac{nrr}{sumlim}\cdot(r_{SD}\cdot SDetN + r_{LD}\cdot LDetN)\cdot R_{NO_3:NH_4} \\ &\quad -SoxNO_3 \end{aligned} \tag{B2}$$

where $R_{NO_3:N} = 106/8$ is the stoichiometry between NO_3 and N in equation (A2). $\mu_{\max} = \mu_{0P}\cdot 1.066^T$ is the growth rate of phytoplankton with T the temperature in °C [*Eppley*, 1972]. L_L is the nondimensional light limitation based on *Evans and Parslow* [1985]

$$L_L = \frac{\alpha I}{\sqrt{(\mu_{\max})^2 + \alpha^2 I^2}}$$

where α represents the initial slope of the photosynthesis-light (P-I) curve. L_{NO_3} is nutrient limitation term for nitrate as described by *Fennel et al*. [2006]

$$L_{NO_3} = \frac{NO_3}{k_{NO_3} + NO_3}\cdot\frac{1}{1 + NH_4/k_{NH_4}}$$

Detailed descriptions and values for the model parameters are listed in Table B1.

Nitrite source and sink terms:

$$\begin{aligned} sms(NO_2) &= +\text{nitrification1} - \text{nitrification2} + \text{denitrification1} \\ &\quad -\text{denitrification2} - \text{anammox} \\ &\quad +\text{chemolitoautotrophic nitrate reduction} \\ &\quad -\text{chemolitoautotrophic nitrite reduction} \\ sms(NO_2) &= +n1\cdot NH_4 - n2\cdot NO_2 + \frac{nrr}{sumlim} \\ &\quad \cdot(r_{SD}\cdot SDetN + r_{LD}\cdot LDetN)\cdot R1_{NO_2:NH_4} \\ &\quad -\frac{dfr}{sumlim}\cdot(r_{SD}SDet + r_{LD}LDet)\cdot R2_{NO_2:NH_4} \\ &\quad -K_{MX}\cdot NH_4\cdot NO_2\cdot\frac{kinhO_{2\_df}}{kinhO_{2\_df} + O_2} \\ &\quad +SoxNO_3 - SoxNO_2 \end{aligned} \tag{B3}$$

where K_{MX} is the anammox rate. $R1_{NO_2:N} = 106/8$ and $R2_{NO_2:N} = 106/12$ are the stoichiometry of NO_2 to N in equations (A2) and (A3), respectively.

Ammonium source and sink terms:

$$\begin{aligned} sms(NH_4) &= -\text{uptake by phytoplankton} - \text{nitrification1} \\ &\quad -\text{anammox} \\ &\quad +\text{zooplankton excretion due to basal metabolism} \\ &\qquad \text{and assimilation} \\ &\quad +\text{detritus remineralization to } NH_4 \\ sms(NH_4) &= -\mu_{\max}\cdot L_L\cdot L_{NH_4}\cdot Phy - n1\cdot NH_4 \\ &\quad -K_{MX}\cdot NH_4\cdot NO_2\cdot\frac{kinhO_{2\_df}}{kinhO_{2\_df} + O_2} \\ &\quad +\left(I_{BM} + I_E\cdot\beta\cdot\left(\frac{Phy^2}{k_P + Phy^2} + \frac{Diaz^2}{k_P + Diaz^2}\right)\right) \\ &\quad \cdot Zoo + r_{SD}\cdot SDetN + r_{LD}\cdot LDetN \end{aligned}$$

where I_{BM} is the rate of zooplankton excretion due to basal metabolism. I_E is the excretion rate which is proportional to the assimilation of ingested phytoplankton and diazotroph. L_{NH_4} is the nutrient limitation term of ammonium as parameterized by *Fennel et al*. [2006]

$$L_{NH_4} = \frac{NH_4}{k_{NH_4} + NH_4}$$

Phosphate source and sink terms:

$$\begin{aligned} sms(PO_4) = &-\text{uptake by phytoplankton} - \text{uptake by diazotrophs} \\ &+ \text{detritus remineralization to } PO_4 \end{aligned}$$

$$\begin{aligned} sms(PO_4) = &-\mu_{\max}\cdot L_L\cdot \min\left(L_{PO_{4Phy}}, L_{NO_3} + L_{NH_4}\right)\cdot Phy\cdot R1_{P:N} \\ &- \mu_{\max D}\cdot L_L\cdot L_{PO_{4Diaz}}\cdot Diaz\cdot R2_{P:N} \\ &+ (r_{SD}\cdot SDetP + r_{LD}\cdot LDetP) \end{aligned}$$

where $\mu_{\max D} = \mu_{0D}\cdot 1.066^T$ is the growth rate of diazotrophs. $L_{PO_4\_Phy}$ and $L_{PO_4\_Diaz}$ are Michaelis-Menten type nutrient limitation terms for phosphate uptake by phytoplankton and diazotroph, respectively:

$$L_{PO_4\_Phy} = PO_4/\left(k_{PO4\_Phy} + PO_4\right) \tag{B6}$$

$$L_{PO_4\_Diaz} = PO_4/(k_{PO4\_Diaz} + PO_4) \tag{B7}$$

Oxygen source and sink terms:

$$\begin{aligned} sms(O_2) = &+\text{phytoplanktonic growth} - \text{nitrification1} \\ &-\text{nitrification2} \\ &- \text{zooplankton basal metabolism and assimilation} \\ &-\text{detritus oxic respiration} \\ &- \text{sulfide oxidation} + O_2 \text{ gas exchange} \end{aligned}$$

$$\begin{aligned} sms(O_2) = &+\mu_{\max}\cdot L_L\cdot \min\left(L_{PO_4\_Phy}, (L_{NO_3} + L_{NH_4})\right)\cdot R_{O:N}\cdot Phy \\ &+ \mu_{\max D}\cdot L_L\cdot L_{PO_4\_Diaz}\cdot R_{O:N}\cdot Diaz - R1_{O_2}\cdot n1\cdot NH_4 \\ &-R2_{O_2}\cdot n2\cdot NO_2 \\ &- \left(I_{BM} + I_E\cdot\beta\cdot\left(\frac{Phy^2}{k_P + Phy^2} + \frac{Diaz^2}{k_P + Diaz^2}\right)\right)\cdot R_{O:N}\cdot Zoo \\ &- \frac{oxr}{sumlim}\cdot(r_{SD}\cdot SDetN + r_{LD}\cdot LDetN)\cdot R_{O:N} \\ &-SoxO_2\cdot R_{S:O} + r_{ge}(O_{2_{sat}} - O_2) \end{aligned}$$

where $R_{O:N} = 106/16$ is the stoichiometry of O_2 to N in equation (A1). $R_{S:O}$ is the stoichiometry of O_2 to H_2S in equation (A9). $R1_{O_2} = 1.5$ and $R2_{O_2} = 0.5$ are the mol O_2 consumed in ammonium and nitrite oxidation, respectively. r_{ge} is the oxygen gas exchange rate and is calculated by $r_{ge} = fO_2/\Delta z_{top}$ where Δz_{top} is the height of the top layer. The gas exchange coefficient is approximated by $fO_2 = 0.31\cdot u_{10}\cdot\sqrt{660/Sc}$ where u_{10} is the wind speed and Sc is the Schmidt number as given by *Wanninkhof* [1992].

Sulfide source and sink terms:

$$\begin{aligned} sms(H_2S) = &+\text{sulfate reduction} - \text{sulfide oxidation by oxygen} \\ &-\text{sulfide oxidation by nitrate} \\ &- \text{sulfide oxidation by nitrite} \end{aligned}$$

$$\begin{aligned} sms(H_2S) = &+\frac{srr}{sumlim}\cdot(r_{SD}\cdot SDetN + r_{LD}\cdot LDetN)\cdot R_{S:NH_4} \\ &-SoxO_2 - SoxNO_3\cdot R_{S:NO_3} \\ &- SoxNO_2\cdot R_{S:NO_2} \end{aligned} \tag{B9}$$

where $R_{S:N} = 53/16$ is stoichiometry of H_2S to N in sulfate reduction of equation (A4). $R_{S:NO_3}$ is the stoichiometry of H_2S to NO_3 in equation (A10). $R_{S:NO_2}$ is the stoichiometry of H_2S to NO_2 in equation (A11).

Phytoplankton source and sink terms:

$$\begin{aligned} sms(Phy) = &+\text{phytoplankton growth} - \text{grazing} \\ &-\text{phytoplankton mortality} \\ &-\text{aggregation with small detritus to large detritus} \\ &-\text{vertical sinking} \end{aligned}$$

$$\begin{aligned} sms(Phy) = &+\mu_{\max}\cdot L_L\cdot \min\left(L_{PO_4\_Phy}, L_{NO_3} + L_{NH_4}\right)\cdot Phy - g_P\cdot Zoo \\ &- m_P\cdot Phy - \tau\cdot(SDetN + Phy)\cdot Phy - w_P\cdot\frac{\partial Phy}{\partial z} \end{aligned} \tag{B10}$$

where g_P is the rate of phytoplankton grazing by zooplankton represented by

$$g_P = g_{\max P}\cdot\frac{Phy^2}{k_P + Phy^2} \tag{B11}$$

with $g_{\max P}$ as maximum rate of the grazing. m_P is the mortality rate of phytoplankton. The constant sinking velocity of phytoplankton is represented by w_P.

Nitrogen-fixing diazotrophs source and sink terms:

$$\begin{aligned} sms(Diaz) = &+\text{diazotroph growth} - \text{grazing} - \text{diazotroph} \\ &\text{mortality} \\ &-\text{vertical sinking}\backslash \end{aligned}$$

$$sms(Diaz) = +\mu_{\max D}\cdot L_L\cdot L_{PO_4\_Diaz}\cdot Diaz - g_D\cdot Zoo - m_D\cdot Diaz - w_P\cdot\frac{\partial Diaz}{\partial z} \tag{B12}$$

where the rate of diazotroph grazing by zooplankton, g_D, is determined by

$$g_D = g_{\max D}\cdot\frac{Diaz^2}{k_P + Diaz^2} \tag{B13}$$

with the maximum grazing rate of $g_{\max D}$. Diazotroph mortality rate is represented by m_D.

Chlorophyll source and sink terms:

$$\begin{aligned} sms(Chl) = &+\text{chlorophyll production} - \text{grazing} \\ &-\text{phytoplankton mortality} \\ &-\text{aggregation with small detritus to large detritus} \\ &-\text{vertical sinking} \end{aligned}$$

$$\begin{aligned} sms(Chl) = &+\rho_{Chl}\cdot\mu_P\cdot Chl - \left(g_P\cdot\frac{Chl}{Phy} + g_D\cdot\frac{Chl}{Diaz}\right)\cdot Zoo \\ &-m_P\cdot Phy - m_D\cdot Diaz \\ &-\tau\cdot(SDetN + Phy)\cdot Chl - w_P\cdot\frac{\partial Chl}{\partial z} \end{aligned}$$

The fraction of phytoplankton growth to chlorophyll synthesis, ρ_{Chl}, is modified from *Geider et al*. [1997] to include the contribution from diazotrophs. Therefore, the fraction is expressed by

$$\rho_{Chl} = \frac{\theta_{\max}(\mu_P Phy + \mu_D Diaz)}{\alpha I Chl} \tag{B15}$$

where $\theta_{\max}$ is the chlorophyll to phytoplanktonic maximum ratio. $\mu_P = \mu_{\max}\cdot L_L\cdot\min\left(L_{PO_4\_Phy}, L_{NO_3} + L_{NH_4}\right)$ and $\mu_D = \mu_{\max D}\cdot L_L\cdot L_{PO_4\_Diaz}$ are the growth rate of phytoplankton and diazotroph, respectively.

Zooplankton source and sink terms:

$$\begin{aligned} sms(Zoo) = {} & +\text{fraction of ingested planktonic assimilation} \\ & -\text{basal metabolism and assimilation-dependent excretion} \\ & -\text{mortality} \end{aligned}$$

$$\begin{aligned} sms(Zoo) = {} & +(g_P + g_D)\cdot\beta\cdot Zoo \\ & -\left(l_{BM} + l_E\cdot\beta\cdot\left(\frac{Phy^2}{k_P + Phy^2} + \frac{Diaz^2}{k_P + Diaz^2}\right)\right)\cdot Zoo \\ & - m_Z\cdot Zoo^2 \end{aligned}$$

where m_Z is the zooplankton mortality rate.

Small detritus nitrogen source and sink terms:

$$\begin{aligned} sms(SDetN) = {} & +\text{fraction of phytoplanktonic egestion} \\ & +\text{phytoplankton, diazotroph, and zooplankton mortality} \\ & -\text{aggregration with phytoplankton to large detritus N} \\ & -\text{remineralization} - \text{vertical sinking} \end{aligned}$$

$$\begin{aligned} sms(SDetN) = {} & +(g_P + g_D)\cdot(1-\beta)\cdot Zoo \\ & +m_P\cdot Phy + m_D\cdot Diaz + m_Z\cdot Zoo^2 \\ & -\tau\cdot(SDetN + Phy)\cdot SDetN - r_{SD}\cdot SDetN \\ & -w_S\cdot\frac{\partial SDetN}{\partial z} \end{aligned} \tag{B17}$$

where τ is the aggregation factor of phytoplankton and small detritus to large detritus. w_S is the constant sinking velocity of small detritus.

Small detritus phosphorus source and sink terms:

$$\begin{aligned} sms(SDetP) = {} & +\text{fraction of phytoplanktonic egestion} \\ & +\text{phytoplankton, diazotroph, and zooplankton mortality} \\ & -\text{aggregration with phytoplankton to large detritus P} \\ & -\text{remineralization} - \text{vertical sinking} \end{aligned}$$

$$\begin{aligned} sms(SDetP) = {} & +(g_P\cdot R1_{P:N} + g_D\cdot R2_{P:N})\cdot(1-\beta)\cdot Zoo \\ & +m_P\cdot Phy\cdot R1_{P:N} \\ & +m_D\cdot Diaz\cdot R2_{P:N} + m_Z\cdot Zoo^2\cdot R1_{P:N} \\ & -\tau\cdot(SDetP + Phy\cdot R1_{P:N})\cdot SDetP - r_{SD}\cdot SDetP \\ & -w_S\cdot\frac{\partial SDetP}{\partial z} \end{aligned}$$

Large detritus nitrogen source and sink terms:

$$\begin{aligned} sms(LDetN) = {} & +\text{aggregration of phytoplankton and small detritus N} \\ & -\text{remineralization} - \text{vertical sinking} \end{aligned}$$

$$sms(LDetN) = +\tau\cdot(SDetN + Phy)^2 - r_{LD}\cdot LDetN - w_L\cdot\frac{\partial LDetN}{\partial z} \tag{B19}$$

where w_L is the constant vertical velocity of large detritus.

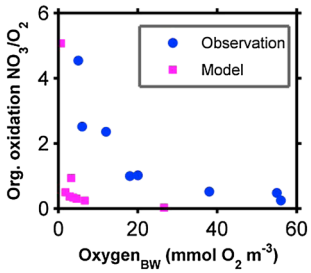

Figure C1. Comparison between the ratio of organic carbon oxidation by nitrate and oxygen as a function of bottom water oxygen concentration as observed by *Canfield* [1993] (blue dot) and as simulated by the implementation of bottom boundary condition in the model (magenta square). Only for this comparison, the narrow shelf width in the Chilean upwelling is extended and used as bottom boundary (~ 70 km shelf width with a steep slope from 100 m shelf break depth to 1000 m). The model results are taken from the shallowest depth (30 m) at the coast to ~500 m depth offshore. The model results show a stronger inhibition of the oxygen for the carbon oxidation by nitrate compared to the observed data. This is because the model uses a low half-saturation constant for oxygen limitation and inhibition term in oxic respiration and heterotrophic nitrate reduction, respectively, based on a recent study by *Thamdrup et al.* [2012] in the Chile OMZ (Table 2).

Large detritus phosphorus source and sink terms:

$$\begin{aligned} sms(LDetP) = &+\text{aggregration of} \\ &\quad \text{phytoplankton} \\ &\quad \text{and small detritus P} \\ &- \text{remineralization} \\ &-\text{vertical sinking} \end{aligned}$$

$$\begin{aligned} sms(LDetP) = &+\tau\cdot(SDetP + Phy\cdot R1_{P:N})^2 \\ &- r_{LD}\cdot LDetP \\ &- w_L\cdot\frac{\partial LDetP}{\partial z} \end{aligned} \tag{B20}$$

Appendix C: Biochemical Bottom Boundary Condition

The model assumes that all sinking organic matter is instantaneously remineralized once it touches the bottom boundary. The fractions of organic matter being remineralized by oxic remineralization, denitrification, or sulfate reduction are controlled by the fraction parameter equations (A5) to (A8). The flux of organic nitrogen and phosphorus at the bottom, $F_{OM\_BottomN}$ and $F_{OM\_BottomP}$ respectively, is:

$$\begin{aligned} F_{OM\_BottomN} = &+w_P\cdot\left.\frac{\partial Phy}{\partial z}\right|_{z=bottom} + w_P\cdot\left.\frac{\partial Diaz}{\partial z}\right|_{z=bottom} \\ &+ w_S\cdot\left.\frac{\partial SDetN}{\partial z}\right|_{z=bottom} + w_L\cdot\left.\frac{\partial LDetN}{\partial z}\right|_{z=bottom} \end{aligned} \tag{C1}$$

$$\begin{aligned} F_{OM\_BottomP} = &+w_P\cdot\left.\frac{\partial Phy}{\partial z}\right|_{z=bottom}\cdot R1_{P:N} + w_P\cdot\left.\frac{\partial Diaz}{\partial z}\right|_{z=bottom}\cdot R2_{P:N} \\ &+ w_S\cdot\left.\frac{\partial SDetP}{\partial z}\right|_{z=bottom} + w_L\cdot\left.\frac{\partial LDetP}{\partial z}\right|_{z=bottom} \end{aligned} \tag{C2}$$

Therefore,

$$\left.\frac{\partial NH_4}{\partial t}\right|_{Z=bottom} = +F_{OM\_BottomN} \tag{C3}$$

$$\left.\frac{\partial PO_4}{\partial t}\right|_{Z=bottom} = +F_{OM\_BottomP} \tag{C4}$$

$$\left.\frac{\partial O_2}{\partial t}\right|_{Z=bottom} = -F_{OM\_BottomN}\cdot\frac{oxr}{sumlim}\cdot R_{O:N} \tag{C5}$$

$$\left.\frac{\partial NO_2}{\partial t}\right|_{Z=bottom} = +F_{OM\_BottomN}\cdot\left(\frac{nrr}{sumlim}\cdot R1_{NO_2:NH_4} - \frac{dfr}{sumlim}\cdot R2_{NO_2:NH_4}\right) \tag{C6}$$

$$\left.\frac{\partial NO_3}{\partial t}\right|_{Z=bottom} = -F_{OM\_BottomN}\cdot\frac{nrr}{sumlim}\cdot R_{NO_3:NH_4} \tag{C7}$$

$$\left.\frac{\partial H_2S}{\partial t}\right|_{Z=bottom} = -F_{OM\_BottomN} \cdot \frac{srr}{sumlim} \cdot R_{S:NH_4} \quad \text{(C8)}$$

Acknowledgments
We wish to thank the Danish National Research Foundation (grant number DNRF53), the Agouron Institute, the European Research Council (ERC, grant number 267233), and the Danish Council for Independent Research (0602-00602B) for financial support. Azhar and Bjerrum are thankfull for free CPU time at the Danish Center for Scientific Computing at Aalborg University.

References

Altabet, M. A., E. Ryabenko, L. Stramma, D. W. R. Wallace, M. Frank, P. Grasse, and G. Lavik (2012), An eddy-stimulated hotspot for fixed nitrogen-loss from the Peru oxygen minimum zone, *Biogeosciences*, *9*(12), 4897–4908, doi:10.5194/bg-9-4897-2012.

Anderson, J. J., A. Okubo, A. S. Robbins, and F. A. Richards (1982), A Model for Nitrite and Nitrate Distributions in Oceanic Oxygen Minimum Zones, *Deep Sea Res., Part I*, *29*(9), 1113–1140.

Barber, R. T., and R. L. Smith (1981), Coastal upwelling ecosystems, in *Analysis of Marine Ecosystems*, pp. 31–68, Academic Press, London.

Blanco, J. L., A. C. Thomas, M. E. Carr, and P. T. Strub (2001), Seasonal climatology of hydrographic conditions in the upwelling region off northern Chile, *J. Geophys. Res.*, *106*(C6), 11,451–11,467.

Bruchert, V., B. B. Jorgensen, K. Neumann, D. Riechmann, M. Schlosser, and H. Schulz (2003), Regulation of bacterial sulfate reduction and hydrogen sulfide fluxes in the central Namibian coastal upwelling zone, *Geochim. Cosmochim. Acta*, *67*(23), 4505–4518, doi:10.1016/S0016-7037(03)00275-8.

Canfield, D. E. (1993), Organic matter oxidation in marine sediments, in *Interactions of C, N, P and S Biogeochemical Cycles and Global Change*, edited by R. Wollast, F. T. Mackenzie, and L. Chou, pp. 333–363, Springer, Berlin.

Canfield, D. E. (2006), Models of oxic respiration, denitrification and sulfate reduction in zones of coastal upwelling, *Geochim. Cosmochim. Acta*, *70*(23), 5753–5765, doi:10.1016/j.gca.2006.07.023.

Canfield, D. E., E. Kristensen, and B. Thamdrup (2005), Aquatic Geomicrobiology, *Advances in Marine Biology*, vol. 48, Elsevier Academic Press, Amsterdam.

Canfield, D. E., F. J. Stewart, B. Thamdrup, L. De Brabandere, T. Dalsgaard, E. F. Delong, N. P. Revsbech, and O. Ulloa (2010), A Cryptic Sulfur Cycle in Oxygen-Minimum-Zone Waters off the Chilean Coast, *Science*, *330*(6009), 1375–1378, doi:10.1126/science.1196889.

Carr, M. E., and E. J. Kearns (2003), Production regimes in four Eastern Boundary Current systems, *Deep Sea Res., Part II*, *50*(22–26), 3199–3221, doi:10.1016/j.dsr2.2003.07.015.

Chaigneau, A., G. Eldin, and B. Dewitte (2009), Eddy activity in the four major upwrelling systems from satellite altimetry (1992–2007), *Prog. Oceanogr.*, *83*(1–4), 117–123, doi:10.1016/j.pocean.2009.07.012.

Chaigneau, A., M. Le Texier, G. Eldin, C. Grados, and O. Pizarro (2011), Vertical structure of mesoscale eddies in the eastern South Pacific Ocean: A composite analysis from altimetry and Argo profiling floats, *J. Geophys. Res.*, *116*, C11025, doi: 10.1029/2011JC007134.

Chapman, D. C. (1985), Numerical Treatment of Cross-Shelf Open Boundaries in a Barotropic Coastal Ocean Model, *J. Phys. Oceanogr.*, *15*(8), 1060–1075.

Chapman, P., and L. V. Shannon (1985), The Benguela Ecosystem 2. Chemistry and Related Processes, *Oceanogr. Mar. Biol.*, *23*, 183–251.

Codispoti, L. A., and F. A. Richards (1976), Analysis of Horizontal Regime of Denitrification in Eastern Tropical North Pacific, *Limnol. Oceanogr.*, *21*(3), 379–388.

Codispoti, L. A., et al. (1986), High Nitrite Levels Off Northern Peru - A Signal of Instability in the Marine Denitrification Rate, *Science*, *233*(4769), 1200–1202, doi:10.1126/science.233.4769.1200.

Colas, F., J. McWilliams, X. Capet, and J. Kurian (2011), Heat balance and eddies in the Peru-Chile current system, *Clim. Dyn.*, *39*(1–21), 509–529 , doi:10.1007/S00382-011-1170-6.

Csanady, G. T. (1990), Physical basis of coastal productivity: The SEEP and MASAR experiments, *Eos Trans. AGU*, *71*(36), 1060–1065.

Dalsgaard, T., D. E. Canfield, J. Petersen, B. Thamdrup, and J. Acuna-Gonzalez (2003), N-2 production by the anammox reaction in the anoxic water column of Golfo Dulce, Costa Rica, *Nature*, *422*(6932), 606–608, doi:10.1038/nature01526.

Dalsgaard, T., B. Thamdrup, L. Farias, and N. P. Revsbech (2012), Anammox and denitrification in the oxygen minimum zone of the eastern South Pacific, *Limnol. Oceanogr.*, *57*(5), 1331–1346, doi:10.4319/lo.2012.57.5.1331.

De Brabandere, L., D. E. Canfield, T. Dalsgaard, G. E. Friederich, N. P. Revsbech, O. Ulloa, and B. Thamdrup (2013), Vertical partitioning of nitrogen-loss processes across the oxic-anoxic interface of an oceanic oxygen minimum zone, *Environ. Microbiol.*, doi:10.1111/1462-2920.12255.

Eppley, R. W. (1972), Temperature and Phytoplankton Growth in Sea, *Fish B-Noaa*, *70*(4), 1063–1085.

Escribano, R., et al. (2004), Biological and chemical consequences of the 1997–1998 El Nino in the Chilean coastal upwelling system: A synthesis, *Deep Sea Res., Part II*, *51*(20–21), 2389–2411, doi:10.1016/j.dsr2.2004.08.011.

Evans, G. T., and J. S. Parslow (1985), A model of annual plankton cycles, *Biol. Oceanogr.*, *3*, 327–347.

Fennel, K., Y. H. Spitz, R. M. Letelier, M. R. Abbott, and D. M. Karl (2002), A deterministic model for N(2) fixation at stn ALOHA in the subtropical North Pacific Ocean, *Deep Sea Res., Part II*, *49*(1–3), 149–174.

Fennel, K., J. Wilkin, J. Levin, J. Moisan, J. O'Reilly, and D. Haidvogel (2006), Nitrogen cycling in the Middle Atlantic Bight: Results from a three-dimensional model and implications for the North Atlantic nitrogen budget, *Global Biogeochem Cycle*, *20*, GB3007, doi: 10.1029/2005GB002456.

Fennel, K., J. Hu, A. Laurent, M. Marta-Almeida, and R. Hetland (2013), Sensitivity of hypoxia predictions for the northern Gulf of Mexico to sediment oxygen consumption and model nesting, *J Geophys Res. Oceans*, *118*, 990–1002, doi:10.1002/jgrc.20077.

Fernandez, C., L. Farías, and O. Ulloa (2011), Nitrogen Fixation in Denitrified Marine Waters, *Plos One*, *6*(6), e20539, doi: 10.1371/journal.pone.0020539.

Flather, R. A. (1976), A tidal model of the northwest European continental shelf, *Memo. Soc. R. Sci. Liege*, *6*(10), 141–164.

Garcia, H. E., R. A. Locarnini, T. P. Boyer, and J. I. Antonov (2006), World Ocean Atlas 2005, in *Nutrients (phosphate, nitrate, silicate)*, NOAA Atlas NESDIS 64, vol. 4, edited by S. Levitus, 396 pp., U.S. Government Printing Office, Washington, D. C.

Geider, R. J., H. L. MacIntyre, and T. M. Kana (1997), Dynamic model of phytoplankton growth and acclimation: Responses of the balanced growth rate and the chlorophyll a:carbon ratio to light, nutrient-limitation and temperature, *Mar. Ecol. Prog. Ser.*, *148*(1–3), 187–200.

Gruber, N., and J. L. Sarmiento (1997), Global patterns of marine nitrogen fixation and denitrification, *Global Biogeochem Cycle*, *11*(2), 235–266 .

Gruber, N., H. Frenzel, S. C. Doney, P. Marchesiello, J. C. McWilliams, J. R. Moisan, J. J. Oram, G. K. Plattner, and K. D. Stolzenbach (2006), Eddy-resolving simulation of plankton ecosystem dynamics in the California Current System, *Deep Sea Res., Part I*, *53*(9), 1483–1516, doi:10.1016/j.dsr.2006.06.005.

Haidvogel, D. B., et al. (2008), Ocean forecasting in terrain-following coordinates: Formulation and skill assessment of the Regional Ocean Modeling System, *J. Comput. Phys.*, *227*(7), 3595–3624, doi:10.1016/j.jcp.2007.06.016.

Jensen, M. M., J. Petersen, T. Dalsgaard, and B. Thamdrup (2009), Pathways, rates, and regulation of N2 production in the chemocline of an anoxic basin, Mariager Fjord, Denmark, *Mar. Chem.*, *113*(1–2), 102–113, doi:10.1016/j.marchem.2009.01.002.

Jin, X., C. Dong, J. Kurian, J. C. McWilliams, D. B. Chelton, and Z. Li (2009), SST–Wind Interaction in Coastal Upwelling: Oceanic Simulation with Empirical Coupling, *J. Phys. Oceanogr.*, *39*(11), 2957–2970, doi:10.1175/2009jpo4205.1.

Jørgensen, B. B. (1996), Material flux in the sediment, in *Eutrophication in Coastal Marine Ecosystems, Coastal Estuarine Stud*, vol. 52, edited by B. B. Jørgensen and K. Richardson, pp. 115–135, AGU, Washington, D. C., doi:10.1029/CE052p0115.

Kalvelage, T., M. M. Jensen, S. Contreras, N. P. Revsbech, P. Lam, M. Günter, J. LaRoche, G. Lavik, and M. M. M. Kuypers (2011), Oxygen Sensitivity of Anammox and Coupled N-Cycle Processes in Oxygen Minimum Zones, *Plos One*, *6*(12), e29299, doi:10.1371/journal.pone.0029299.

Kamykowski, D., and S. J. Zentara (1990), Hypoxia in the World Ocean as Recorded in the Historical Data Set, *Deep Sea Res., Part I*, *37*(12), 1861–1874.

Konovalov, S. K., J. W. Murray, G. W. Luther, and B. M. Tebo (2006), Processes controlling the redox budget for the oxic/anoxic water column of the Black Sea, *Deep Sea Res. Part II: Topical Studies in Oceanography*, *53*(17–19), 1817–1841, doi:10.1016/j.dsr2.2006.03.013.

Kuypers, M. M. M., G. Lavik, D. Woebken, M. Schmid, B. M. Fuchs, R. Amann, B. B. Jorgensen, and M. S. M. Jetten (2005), Massive nitrogen loss from the Benguela upwelling system through anaerobic ammonium oxidation, *Proc. Natl. Acad. Sci. U.S.A.*, *102*(18), 6478–6483, doi:10.1073/pnas.0502088102.

Lam, P., and M. M. M. Kuypers (2011), Microbial Nitrogen Cycling Processes in Oxygen Minimum Zones, *Annu. Rev. Mar. Sci.*, *3*(3), 317–345, doi:10.1146/annurev-marine-120709-142814.

Lam, P., G. Lavik, M. M. Jensen, J. van de Vossenberg, M. Schmid, D. Woebken, G. Dimitri, R. Amann, M. S. M. Jetten, and M. M. M. Kuypers (2009), Revising the nitrogen cycle in the Peruvian oxygen minimum zone, *Proc. Natl. Acad. Sci. U.S.A.*, *106*(12), 4752–4757, doi:10.1073/pnas.0812444106.

Large, W. G., J. C. Mcwilliams, and S. C. Doney (1994), Oceanic Vertical Mixing - A Review and a Model with a Nonlocal Boundary-Layer Parameterization, *Rev. Geophys.*, *32*(4), 363–403.

LaRoche, J., and E. Breitbarth (2005), Importance of the diazotrophs as a source of new nitrogen in the ocean, *J. Sea Res.*, *53*(1–2), 67–91, doi:10.1016/j.seares.2004.05.005.

Lavik, G., et al. (2009), Detoxification of sulphidic African shelf waters by blooming chemolithotrophs, *Nature*, *457*(7229), 581–U586, doi:10.1038/Nature07588.

Lipschultz, F., S. C. Wofsy, B. B. Ward, L. A. Codispoti, G. Friedrich, and J. W. Elkins (1990), Bacterial Transformations of Inorganic Nitrogen in the Oxygen-Deficient Waters of the Eastern Tropical South-Pacific Ocean, *Deep Sea Res., Part I*, *37*(10), 1513–1541.

Mahmood, Q., P. Zheng, J. Cai, D. L. Wu, B. L. Hu, and J. Y. Li (2007), Anoxic sulfide biooxidation using nitrite as electron acceptor, *J. Hazard. Mater.*, *147*(1–2), 249–256, doi:10.1016/j.jhazmat.2007.01.002.

Marchesiello, P., J. C. McWilliams, and A. Shchepetkin (2001), Open boundary conditions for long-term integration of regional oceanic models, *Ocean Model*, *3*(1–2), 1–20.

Monteiro, F. M., and M. J. Follows (2009), On the interannual variability of nitrogen fixation in the subtropical gyres, *J. Mar. Res.*, *67*(1), 71–88.

Morel, F. M. M., and J. G. Hering (1993), *Principles and Applications of Aquatic Chemistry*, Wiley, New York.

Olson, R. J. (1981), Differential Photoinhibition of Marine Nitrifying Bacteria - A Possible Mechanism for the Formation of the Primary Nitrite Maximum, *J. Mar. Res.*, *39*(2), 227–238.

Paulmier, A., and D. Ruiz-Pino (2009), Oxygen minimum zones (OMZs) in the modern ocean, *Prog. Oceanogr.*, *80*(3–4), 113–128, doi:10.1016/j.pocean.2008.08.001.

Schmittner, A., A. Oschlies, H. D. Matthews, and E. D. Galbraith (2008), Future changes in climate, ocean circulation, ecosystems, and biogeochemical cycling simulated for a business-as-usual CO(2) emission scenario until year 4000 AD, *Global Biogeochem Cycle*, *22*, Gb1013, doi: 10.1029/2007GB002953.

Shaffer, G. (1989), A Model of Biogeochemical Cycling of Phosphorus, Nitrogen, Oxygen, and Sulfur in the Ocean - One-Step toward a Global Climate Model, *J. Geophys. Res.*, *94*(C2), 1979–2004, doi:10.1029/Jc094ic02p01979.

Shchepetkin, A. F., and J. C. McWilliams (2005), The regional oceanic modeling system (ROMS): A split-explicit, free-surface, topography-following-coordinate oceanic model, *Ocean Model*, *9*(4), 347–404, doi:10.1016/j.ocemod.2004.08.002.

Soetaert, K., P. M. J. Herman, and J. J. Middelburg (1996), Dynamic response of deep-sea sediments to seasonal variations: A model, *Limnol. Oceanogr.*, *41*(8), 1651–1668.

Thamdrup, B., T. Dalsgaard, M. M. Jensen, O. Ulloa, L. Farias, and R. Escribano (2006), Anaerobic ammonium oxidation in the oxygen-deficient waters off northern Chile, *Limnol. Oceanogr.*, *51*(5), 2145–2156.

Thamdrup, B., T. Dalsgaard, and N. P. Revsbech (2012), Widespread functional anoxia in the oxygen minimum zone of the Eastern South Pacific, *Deep Sea Res., Part I*, *65*(0), 36–45, doi: 10.1016/j.dsr.2012.03.001.

Thomas, A. C., J. L. Blanco, M. E. Carr, P. T. Strub, and J. Osses (2001), Satellite-measured chlorophyll and temperature variability off northern Chile during the 1996–1998 La Niña and El Niño, *J. Geophys. Res.*, *106*(C1), 899–915, doi:10.1029/1999jc000052.

Van Cappellen, P., J.-F. Gaillard, and C. Rabouille (1993), Biogeochemical Transformations in Sediments: Kinetic Models of Early Diagenesis, in *Interactions of C, N, P, and S Biogeochemical Cycles*, edited by R. Wollast, F. T. Mackenzie, and L. Chou, pp. 401–446, Springer Verlag, NATO-ARW.

Wanninkhof, R. (1992), Relationship between Wind-Speed and Gas-Exchange over the Ocean, *J. Geophys. Res.*, *97*(C5), 7373–7382.

Ward, B. B., H. E. Glover, and F. Lipschultz (1989), Chemoautotrophic activity and nitrification in the oxygen minimum zone off Peru, *Deep Sea Research Part A Oceanogr. Res. Pap.*, *36*(7), 1031–1051, doi:10.1016/0198-0149(89)90076-9.

Ward, B. B., D. G. Capone, and J. P. Zehr (2007), What's New in the Nitrogen Cycle?, *Oceanography*, *20*(2), 101–109.

Wooster, W. S., and M. Gilmartin (1961), The Peru-Chile Undercurrent, *J. Mar. Res.*, *19*(3), 97–122.

Yakushev, E. V., F. Pollehne, G. Jost, I. Kuznetso, B. Schneider, and L. Urnlauf (2007), Analysis of the water column oxic/anoxic interface in the Black and Baltic seas with a numerical model, *Mar. Chem.*, *107*(3), 388–410, doi:10.1016/j.marchem.2007.06.003.

Yool, A., A. P. Martin, C. Fernandez, and D. R. Clark (2007), The significance of nitrification for oceanic new production, *Nature*, *447*(7147), 999–1002, doi:10.1038/nature05885.